

# A New Complete Sample of Sub-millijansky Radio Sources: An Optical and Near-Infrared Study

Frank J. Masci<sup>1,2</sup>, J. J. Condon<sup>3</sup>, T. A. Barlow<sup>1</sup>, C. J. Lonsdale<sup>1</sup>, D. L. Shupe<sup>1</sup>, O. Pevunova<sup>1,4</sup> and F. Fang<sup>1</sup>

Received \_\_\_\_\_; accepted \_\_\_\_\_

---

<sup>1</sup>Infrared Processing and Analysis Center, M/S 100-22, California Institute of Technology, Jet Propulsion Laboratory, Pasadena, CA 91125

<sup>2</sup>Electronic mail: fmasci@ipac.caltech.edu.au

<sup>3</sup>National Radio Astronomy Observatory, 520 Edgemont Road, Charlottesville, VA 22903

<sup>4</sup>Present address: Interferometry Science Group, M/S 171-122C, Jet Propulsion Laboratory, Pasadena, CA 91109-8099

## ABSTRACT

The Very Large Array (VLA) has been used in C-configuration to map an area  $\simeq 0.3 \text{ deg}^2$  at 1.4 GHz with  $5\sigma$  sensitivities over four equal areas of 0.305, 0.325, 0.380 and 0.450 mJy. Radio properties are presented for 62 detected sources. Deep optical imaging to Gunn  $r \simeq 25$  mag using the Hale 5-m telescope covering  $\simeq 0.21 \text{ deg}^2$  is reported for a subset of 43 sources. Archival  $J$ ,  $H$  and  $K$ -band photometry from the Two-Micron All Sky Survey (2MASS) is also presented. Using a robust likelihood ratio algorithm, 26 radio sources were optically identified with probabilities  $P_{id} \gtrsim 80\%$ , nine are uncertain/ambiguous detections and eight are empty fields. Comparisons with a stellar synthesis model which includes radio emission and dust reddening suggests that the near-infrared-to-optical emission in a small, bright sub-sample is reddened by ‘optically thin’ dust with magnitude  $A_V \simeq 2 - 2.5$ , regardless of morphological type. This is consistent with other, more direct determinations. The radio-to-optical(-near-infrared) flux ratios of early-type morphologies require significant contamination in the radio by an active galactic nucleus (AGN). Using our simple modelling approach, we also discuss a potential diagnostic for selecting Ultraluminous Infrared Galaxies (ULIGS) to  $z \simeq 1.6$  from microjansky radio surveys.

*Subject headings:* galaxies: active — galaxies: starburst — cosmology: observations — radio continuum: galaxies

## 1. INTRODUCTION

The advent of deep radio surveys reaching flux densities well below 5 mJy (Windhorst et al. 1985; Oort 1987; Windhorst et al. 1993; Hopkins et al. 1998; Richards 2000) has strikingly revealed a population of faint sources in excess of the ‘normal’ population of radio galaxies. This corresponds to a steepening of the differential source counts re-approaching the Euclidean slope  $S^{-2.5}$  at  $S \lesssim 1\text{mJy}$ , compared to  $\approx S^{-1.9}$  for a non-evolving population in a flat cosmology. The faint counts suggest that significant evolution has occurred over the redshift range spanned by the observed population. Photometric and spectroscopic studies (Thuan et al. 1984; Windhorst et al. 1985; Thuan & Condon 1987; Benn et al. 1993) suggest that the faint excess at 1.4 GHz is composed predominately of star-forming galaxies similar to the nearby starburst population dominating the *Infrared Astronomical Satellite (IRAS)* 60- $\mu\text{m}$  counts (Benn et al. 1993). Indeed, this is supported by the strong correlation between radio (1.4 GHz) and far-infrared (60- $\mu\text{m}$ ) flux densities of galaxies (Helou, Soifer & Rowan-Robinson 1985), implying a significant proportion of starburst galaxies at faint flux levels.

The overall observed source-count distribution from faint ( $\mu\text{Jy}$ ) to bright ( $S_{1.4} \gtrsim 10\text{mJy}$ ) flux densities cannot be explained by starbursts alone. Evolutionary models of radio source counts need to invoke two separate populations (eg. Danese et al. 1987; Rowan-Robinson et al. 1993; Hopkins et al. 1998). Condon (1989) describes these populations as starbursts and monsters, each powered by different mechanisms: ‘starbursts’ deriving their radio emission from supernova remnants and HII regions and ‘monsters’ from compact nuclear related activity (eg. active galactic nuclei; AGNs). The proportion of AGN is much greater at higher flux densities  $S_{1.4} \gtrsim 10\text{ mJy}$  (Kron, Koo & Windhorst 1985; Gruppioni et al. 1998), where a majority are associated with classical radio galaxies exhibiting extended (FRI and FRII-type) morphologies (Fanaroff & Riley 1974). The dominant population at bright

radio flux densities  $S_{1.4} \gtrsim 1$  mJy is comprised mostly of ellipticals while at sub-mJy to  $\mu$ Jy levels, the optical counterparts are identified as blue galaxies exhibiting peculiar (compact, interacting and irregular) morphologies (Kron, Koo & Windhorst 1985; Gruppioni et al. 1998). Despite the dedicated efforts in understanding faint radio sources, there is still no clear understanding of their stellar population, how they evolve with redshift and how they relate to local normal galaxies.

Faint radio-selected surveys are insensitive to the effects of extinction by dust which is known to severely bias surveys at optical/UV wavelengths. This is particularly important for derivations of the cosmic history of star formation and its relation to hierarchical models of galaxy formation. Optical/UV Studies have shown that there is an increase in both the space density of star-forming, morphologically disturbed galaxies and also, the global star formation rate with redshift to  $z \gtrsim 1$  (eg. Madau et al. 1986). Similar evidence is emerging from studies of sub-mm sources (Blain et al. 1999). A similar trend is also starting to appear amongst the faint radio population at  $z \lesssim 1$  - the redshift sampled by the faintest surveys (eg. Cram 1998; Haarsma et al. 1999).

Despite the growing evidence for dust at high redshifts, there is currently no census on whether the global star-formation rates derived from radio observations exceed those determined from optical/UV studies. Most radio studies (eg. Serjeant et al. 1998; Mobasher et al. 1999) claim that dust extinction is unimportant on  $\text{H}\alpha$  and optically derived rates to  $z \sim 1$ . It is likely that the relatively bright optical flux limits required for accurate spectroscopic analysis may be biasing these studies against faint (eg. distant or dusty) objects. Cram et al. (1998) note that systematic discrepancies may exist between the various star formation indicators which are not well understood (see also Schaerer 1999). A direct study of the extinction properties of radio-selected star forming galaxies is therefore necessary before an attempt is made to reconcile star formation rates derived independently

from radio and optical measurements. Indeed, an analysis of Balmer decrements and optical–near-infrared colors in star forming galaxies by Georgakakis et al. (1999) from the Phoenix Deep Survey (Hopkins et al. 1998), finds evidence for visual extinctions from one to a few magnitudes. Currently, about 20% of existing micro-jansky radio samples remain unidentified to  $I = 25$  mag in Hubble Deep Field images (eg. Richards et al. 1999). A majority of these could represent a significant population of dust-enshrouded starbursts and/or AGN at high redshift.

The primary aim of this paper is to introduce a new complete sample of radio sources selected at 1.4 GHz, uniformly selected over the flux range  $S \gtrsim 0.3$  mJy ( $5\sigma$ ) from a homogenous area covering  $\simeq 0.3$  deg $^2$ . The results of deep optical observations and available archival near-infrared data for a subset of the sample is also presented. Although we currently lack valuable spectroscopic information, we combine radio–near-infrared–optical flux ratios, radio maps and optical images to explore the properties of the entire sample. Our deep optical identifications provide the opportunity to asses the importance of dust in star-forming systems via the observed radio–to–optical and near-infrared–to–optical colors. Simple stellar synthesis models that include radio emission and reddening are used to constrain possible amounts of extinction.

This paper is organised as follows. In §2, we discuss the radio observations, data reduction, present the radio catalog and compare our results to existing overlapping large area surveys. The optical photometric observations, their reduction and astrometric calibrations are discussed in §3. Our method for radio-optical identification, archival near-infrared data, radio-optical image overlays and optical/near-infrared catalog are presented in §4. A study of the radio, near-infrared and optical colors, and constraints on synthesis models incorporating dust is presented in §5. An application of our color-color analysis to select high redshift ultraluminous infrared galaxies from deep radio surveys is

discussed in §6. All results and future prospects are summarised in §7.

## 2. RADIO OBSERVATIONS

### 2.1. Strategy

Observations were made with the VLA in C configuration at a frequency of 1.4 GHz on 19 December 1998. This configuration enabled us to achieve optimum resolution, sensitivity and areal coverage. The  $5\sigma$  confusion limit for this configuration is  $50\mu\text{Jy}/\text{beam}$  and at 1.4 GHz, the synthesised beam size (Full Width at Half Power; FWHP) is  $\sim 15$  arcsec. The well defined synthesised beam of the VLA should enable us to pinpoint optical identifications to  $\sim 1$  arcsec, except for extended sources with multiple components. An observing frequency of 1.4 GHz was chosen since it allows us to cover a relatively large area with a small number of pointing centers. At this frequency, the FWHP of the VLA primary beam is 31 arcmin and approximately corresponds to the diameter of our final imaged field. This relatively large areal coverage avoids field-to-field variations in source counts induced by high-redshift clustering, a serious limitation of earlier 1.4 GHz radio surveys of smaller area. Although surveys at higher frequencies (eg. 8 GHz) can reach fainter flux densities than at 1.4GHz, the spectral index of most radio sources,  $\alpha \sim 1$  ( $S \propto \nu^{-\alpha}$ ), implies that the population being sampled is similar.

As usual in surveys based on one or a relatively small number of overlapping pointings, there is increasing attenuation of the primary beam with increasing distance from the field center, i.e., observations become less sensitive near the edges of the field. To correct for this and provide uniform sensitivity over the full area of our field, we observed seven equally spaced pointings arranged in a hexagonal pattern with a separation of  $26'$  between pointing centers. The resulting root mean square (rms) map noise of the combination

of pointings was then nearly constant. This method is currently adopted in large area surveys such as the *NVSS* (NRAO VLA Sky Survey) and discussed in detail by Condon et al. (1998). Our overall field was centered on the pointing RA(2000)= $00^h13^m12^s.0$ , Dec.(2000)= $+25^\circ54'43''.92$ . The integration time of each pointing was  $\sim 1$  hour. This allowed us to reach an optimum rms noise of  $\sim 60\mu\text{Jy}$  in regions free from bright contaminating sources (see § 2.3 for more details).

Our observations were made in spectral line mode using a total bandwidth of 37.5 MHz, compared to 50 MHz usually used in continuum mode. Although a narrower bandwidth means a reduction in sensitivity by about 25% near the pointing centers relative to continuum mode, the effect of bandwidth smearing (i.e. chromatic aberration) is significantly reduced. Bandwidth smearing effectively reduces the area covered by each pointing in continuum mode, making wide-field mapping of uniform sensitivity difficult. Additionally, the spectral line mode is less prone to possible interference noise spikes.

## 2.2. Data Reduction

The data were analysed with the NRAO **AIPS** reduction package. First, the tasks **TVFLG** and **CLIP** were used to delete the corrupted visibility data (eg. bad baselines, high amplitudes from interference *etc*). The tasks **BPASS** and **SPLIT** were then used for the bandpass and flux density calibration respectively. The images for each pointing were then cleaned using the task **IMAGR**. Finally, the **COMB** task was used for combining the seven pointings into a single  $33' \times 33'$  map corrected for primary-beam attenuation.

### 2.3. Noise and Source Extractions

The resulting rms noise of our final map after correcting for primary-beam attenuation was not exactly uniform over the entire field, but found to vary by up to 30%. This is due to the presence of a few strong to moderately strong sources ( $\gtrsim 50$  mJy) near the edges of our field. These tend to contribute significantly to the ‘antenna noise’ temperature rather than the common ‘receiver noise’ temperature, introducing systematic additional noise fluctuations in the output.

Despite this variation in sensitivity, we were able to divide our  $33 \times 33$  arcmin $^2$  field into four equally sized ( $\approx 16.5 \times 16.5$  arcmin $^2$ ) regions within which the rms noise was approximately constant, varying by no more than a few percent. These constant rms noise regions are necessary in order to apply an automated source finding algorithm over a single continuous region (see below). The lowest and highest rms noise amongst these regions was  $\simeq 60.9$   $\mu$ Jy/beam and  $\simeq 90.3$   $\mu$ Jy/beam respectively. See Table 1 for the region definitions. The rms noise of each region was estimated using the amplitude distribution of the pixel values as produced by the AIPS task **IMEAN**. This distribution is usually the sum of a Gaussian noise core with a positive-extended tail caused by discrete sources. The rms of the noise distribution should then be nearly equal to the rms of the distribution obtained by reflecting the negative flux portion of the amplitude distribution about flux=0. In Figure 1, we show the distribution in pixel values of our entire 33' field. The rms deviation in peak flux density derived from a fit to this histogram is  $\simeq 69\mu$ Jy/beam. Figure 2 shows a contour map of our entire radio field.

Each separate constant rms noise region in Table 1 was used for the source extractions. Within each region, we searched for radio sources up to a peak flux density  $\geq 5$  times the rms value of the region. The sources were extracted using the task **SAD** (Search And Destroy) which uses a least square Gaussian fit to estimate the flux, position and size for each

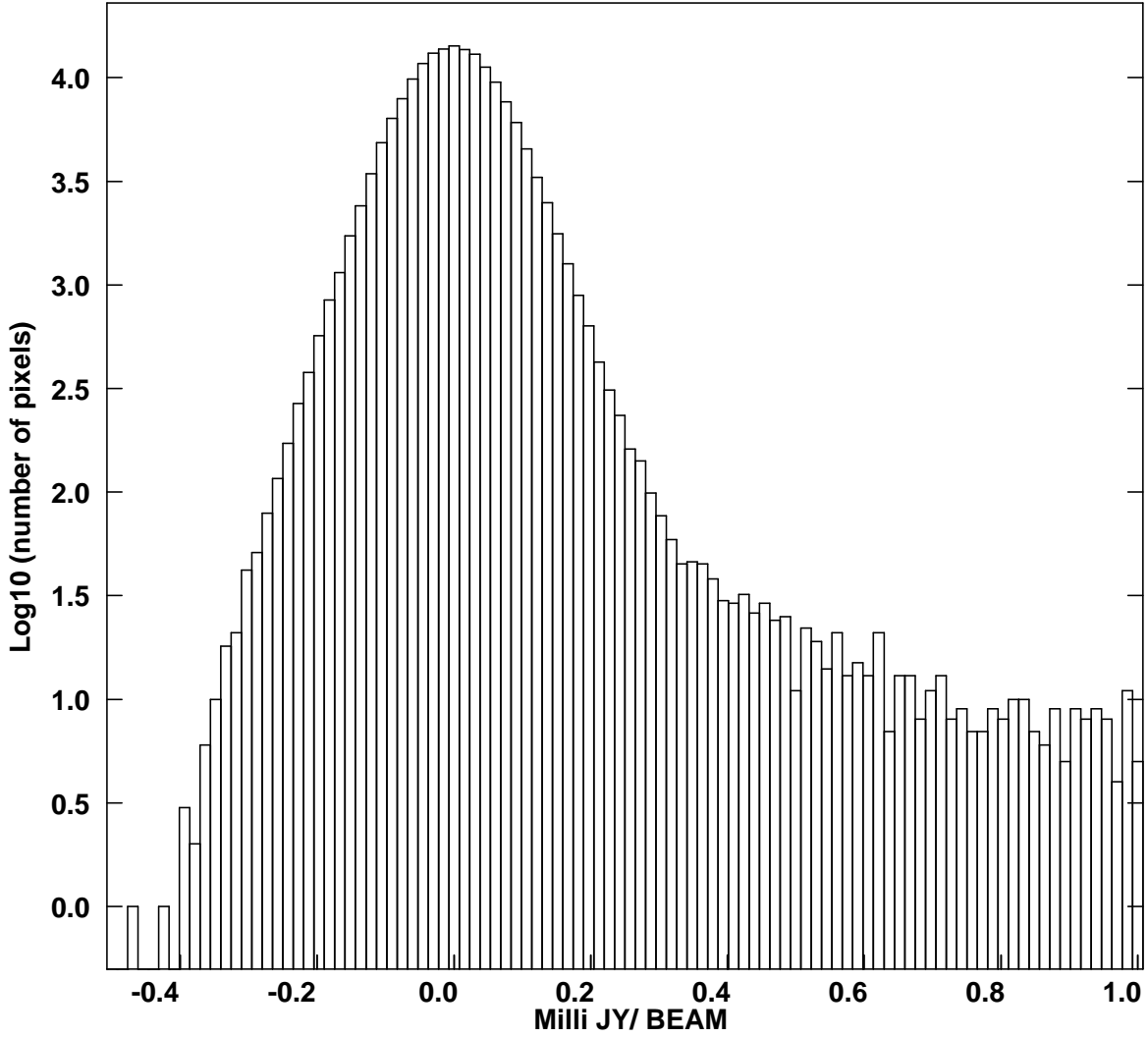


Fig. 1.— Logarithmic histogram of pixel flux densities in our complete radio map.

Fig. 2.— Available at <http://spider.ipac.caltech.edu/staff/fmasci/papers/> (click on “Figure2.ps”). Contour plot of our radio map covering an area  $33 \times 33 \text{ arcmin}^2 = 495 \times 495 \text{ pixels}$ . Contour levels are 0.2, 0.4, 0.6, 0.8, 1.0, 1.2, 1.4, 1.6 mJy/beam. Note the increase in rms noise from the bright off-field source in the top right corner.

selected source. For faint sources however, Gaussian fits are usually unreliable (see Condon 1997). For this reason, we adopted the following method for the source extraction: first, we ran the task **SAD** with a  $3\sigma_{rms}$  detection threshold to obtain an initial list of candidates, we then derived the peak flux densities of the faint sources (with  $3\sigma < S_{peak} < 7\sigma$ ) using the **MAXFIT** task. This task uses a second order interpolation algorithm and is known to be more accurate. Only sources with a **MAXFIT** peak flux density  $\geq 5\sigma_{rms}$  were retained. For these faint sources, the total flux density was estimated using the task **IMEAN**, which integrates the pixel values in a specific rectangle. For all other parameters (sizes, positions and position angles) we retained the values obtained from the initial Gaussian fits. Only two sources had irregular morphologies showing multiple components. For these, the total flux was determined using the task **TVSTAT** which allows an integration over a specific irregular area.

The number of sources detected in each constant rms noise region is summarised in Table 1. A total of 62 sources were detected with flux densities  $\geq 5\sigma_{rms}$  over an area of  $0.303 \text{ deg}^2$ . Table 2 shows the full radio catalog which reports (in column order): the source name; RA and Dec.(J2000); errors in RA and Dec.; the peak flux density  $S_P$ ; error in  $S_P$ ; the total flux density  $S_T$ ; error in  $S_T$ ; the full width half maximum (FWHM) of the major and minor axes  $\theta_M$  and  $\theta_m$ ; the position angle  $PA$  of the major axis (in degrees); and the errors associated with  $\theta_M$ ,  $\theta_m$  and  $PA$  respectively. The different components of multiple sources are labelled “C1” and “C2”. In Figure 3, we show the distribution of peak flux densities and the total to peak flux ratio as a function of peak flux for all sources. Sources with ratios  $S_T/S_P < 1$  in Figure 3b are primarily due to uncertainties on measured fluxes as estimated from the two dimensional Gaussian fits. Uncertainties in both peak and total fluxes are relatively low, reaching no more than  $\approx 5\%$  at the faintest levels. Contour maps of radio sources with available optical data are shown in Figure 8.

(ALL TABLES ARE LOCATED AT THE BACK).

#### 2.4. Comparison with the *NVSS* Catalog

The  $33 \times 33$  arcmin $^2$  region that we observed with the VLA was also covered by the NRAO VLA Sky Survey (*NVSS*). The *NVSS* covers the sky north of  $\delta = -40^\circ$  at 1.4 GHz with 45" resolution and limiting flux density of  $\simeq 2.25$  mJy ( $5\sigma$ ). To this limit, 17 of our sources were found to be in common with the *NVSS* public catalog. A comparison of flux densities derived in this study with those from this catalog is shown in Figure 4. It is evident that our derived flux densities are on average lower than those from the *NVSS*. This was also reported in a larger comparision study by Ciliegi et al. (1999) using a similar observational set-up and can be explained by the difference in resolutions used in the two surveys: 15" vs. 45" for the *NVSS*. High resolution surveys, with smaller synthesised beam sizes tend to lose flux due to a loss in effective surface brightness over the entire beam. Although the effect is only marginal for bright fluxes, it may become important when attempting to detect faint, low-surface brightness objects at high redshift.

### 3. OPTICAL PHOTOMETRIC OBSERVATIONS

#### 3.1. Observations and Data Reduction

Optical CCD photometry of our radio field was carried out on the 5-m Hale telescope at Palomar<sup>5</sup> Observatory during the nights of 27-29 August 1997. These fields were initially acquired for subsequent deep mid-IR imaging with the *Wide Field Infrared Explorer* mission

---

<sup>5</sup>Operated by California Institute of Technology, Pasadena, CA 91125

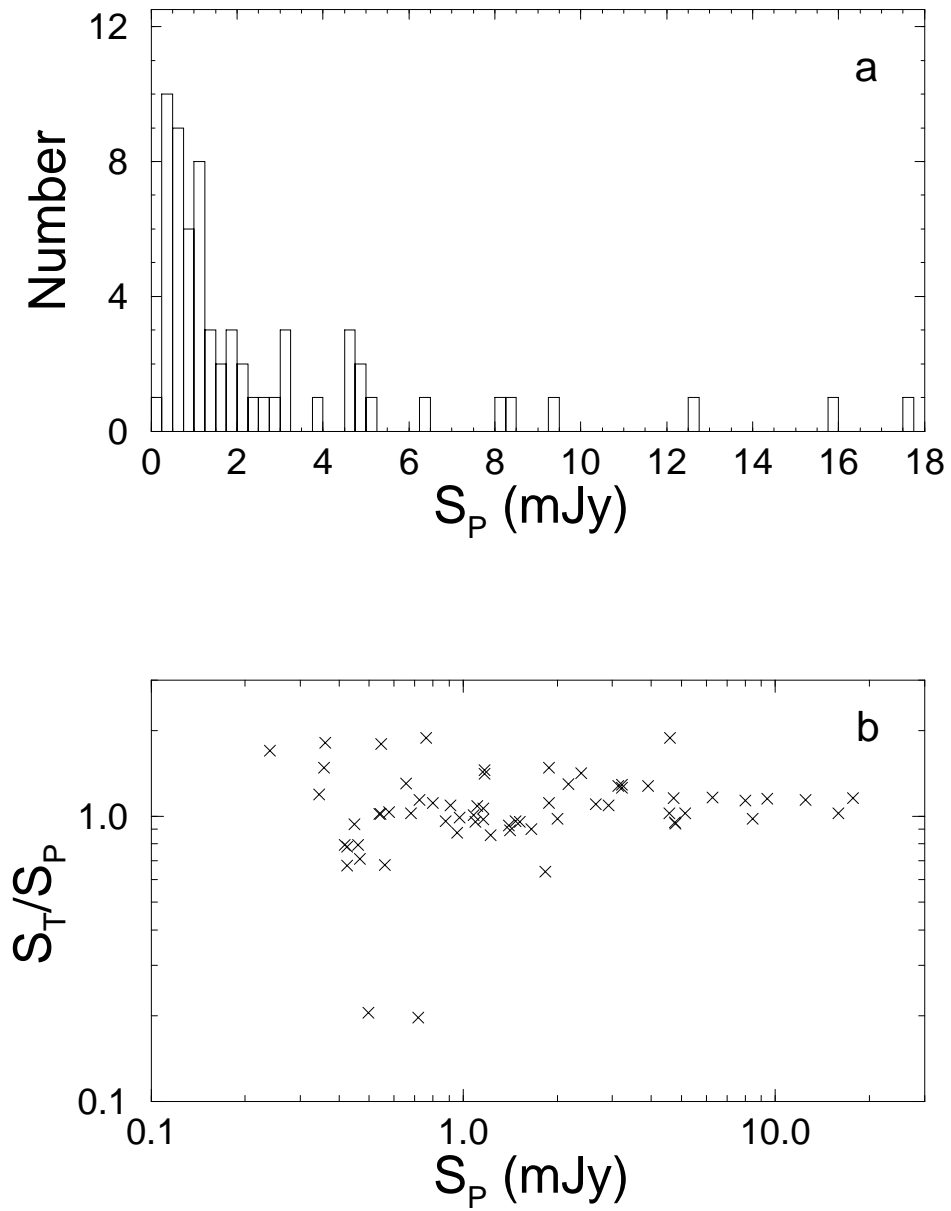


Fig. 3.— (a) Distribution of peak flux density and (b) total to peak flux ratio as a function of peak flux.

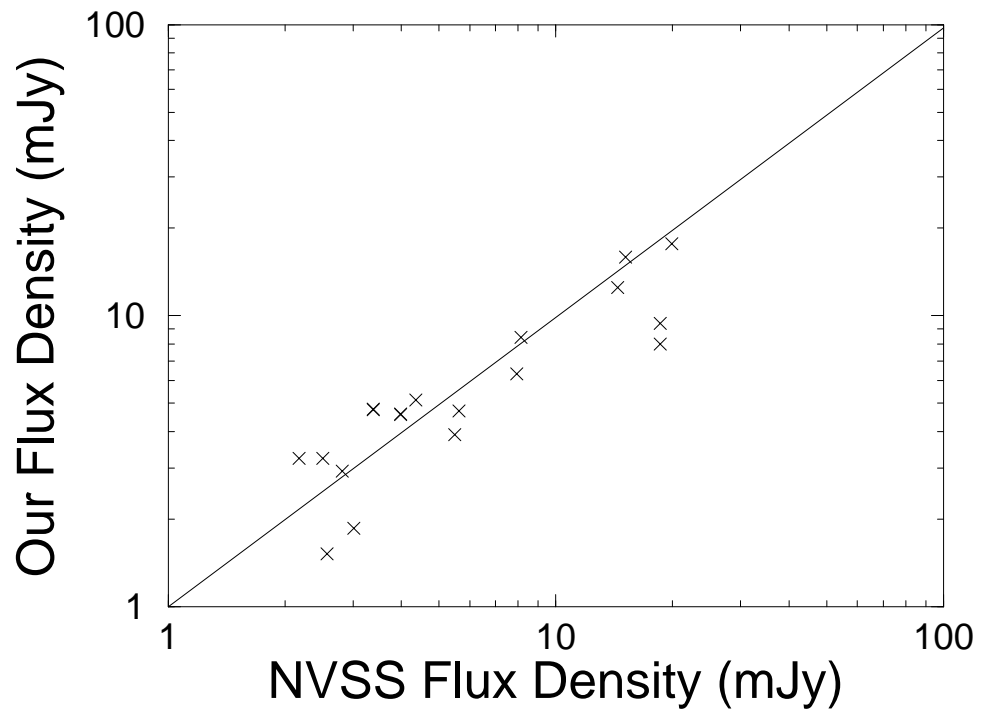


Fig. 4.— The peak flux density obtained with our survey versus that reported for the same sources in the *NVSS* public database.

(*WIRE*), but the mission failed to perform to expectations. The Carnegie Observatories Spectroscopic Multislit and Imaging Camera (COSMIC; Kells et al. 1998) mounted at the  $f/3.5$  prime focus with a TEK 2K CCD was used to image nine  $9.7 \times 9.7 \text{ arcmin}^2$  fields in the Gunn  $r$  (6550Å) filter. Each optical field comprised of three optical pointings offset by  $2'$ , each with integrations of 600 sec giving a total 1800 sec per field. This resulted in a limiting magnitude of  $r \simeq 25$  mag ( $5\sigma$ ). The seeing was relatively good, with typically  $1 - 1.4''$  (FWHM) throughout. The optical fields did not cover our entire  $33 \times 33 \text{ arcmin}^2$  radio field. The nine slightly overlapping optical fields correspond to an areal coverage  $27.5 \times 27 \text{ arcmin}^2$ , or about 67% of the radio map.

The CCD data were reduced using standard tasks in the **IRAF** package. Frames were first debiased, then flat-fielded using dome-flats. Bad pixels and columns were removed by interpolating between adjacent pixels and lastly, the individual dithered frames were median combined to remove cosmic ray hits. Calibration was performed using standard stars from Thuan & Gunn (1976). These were used to correct for atmospheric extinction from varying airmass and provide the instrumental zero point. Photometric uncertainties, estimated using these standards were no more than  $\approx 0.05$  mag.

Sources in the reduced optical frames were extracted using the **DAOPHOT** package in **IRAF** (Stetson 1987). This package has the benefit of performing photometry in crowded fields, which was the case in most regions of our optical fields. The algorithm involves the following steps: first, sources are extracted above a given threshold, given as a multiple of the total CCD noise (sky and read noise,  $\sigma_{tot}$ ). We adopted threshold values of  $4.5-5\sigma_{tot}$ , which was just high enough to avoid large numbers of spurious detections. Second, simple aperture photometry was performed on these identified sources. This required a specification of the aperture radius which is likely to contain most of the light of our target source, and width of a surrounding annulus to estimate and subtract the sky

background. We adopted a radius of six arcsec and annulus width of four arcsec. Next, a point spread function (PSF) was determined in each of our nine fields. This involved an iterative technique to remove contamination from neighbouring sources in crowded fields near our PSF candidates. Simultaneous PSF fitting on all sources was then performed to identify sources which were previously hidden in crowded regions. Finally, the magnitudes determined from PSF fits were aperture corrected to a common aperture size as used on our standard stars. Aperture corrections were typically 0.22 mag. A final visual inspection removed any spurious detections. A total of  $\approx 300$  sources were extracted from each  $9.7 \times 9.7$  arcmin $^2$  field to a limit of  $r \simeq 25$  mag.

### 3.2. Astrometry

The astrometry on the optical images was carried out by locating 10-12 APM catalog stars in each field. The `ccmap` and `cctran` tasks in the `IRAF immcoords` package were used to compute plate solutions from relating pixel positions to astrometric coordinates. Astrometric coordinates for all sources on the frames were then determined. By comparing the positions of several sources common to the APM catalog and our fields, we find that rms position uncertainties were typically  $\lesssim 0.9''$ .

## 4. OPTICAL/NEAR-INFRARED IDENTIFICATION OF RADIO SOURCES

### 4.1. Method for Optical Identification

We assign optical identifications and estimate their reliability using a robust likelihood ratio ( $LR$ ) analysis. This general method has frequently been used to assess identification probabilities for radio and infrared sources (eg. de Ruiter, Willis & Arp 1997; Prestage &

Peacock 1983; Sutherland & Saunders 1992; Lonsdale et al. 1998). The method, which computes the probability that a suggested identification is the ‘true’ optical counterpart, is outlined as follows:

For each optical candidate  $i$ , in a given search area of some radio source  $j$ , we calculate the value of the dimensionless difference in radio and optical positions:

$$r_{ij} = \left[ \frac{(\alpha_i - \alpha_j)^2}{\sigma_{\alpha_i}^2 + \sigma_{\alpha_j}^2} + \frac{(\delta_i - \delta_j)^2}{\sigma_{\delta_i}^2 + \sigma_{\delta_j}^2} \right]^{1/2}, \quad (1)$$

where the  $\alpha$ ’s and  $\delta$ ’s represent right ascensions and declinations respectively, and  $\sigma$ ’s standard deviations. As a conservative measure, we assume a moderately large search radius of  $10''$ , chosen to allow for the maximal position uncertainties:  $\sigma_{\text{opt}} \approx 1.4''$  and  $\sigma_{\text{rad}} \approx 1.5''$  (assuming  $5\sigma_{\text{eff}}$ , where  $\sigma_{\text{eff}} = (\sigma_{\text{opt}}^2 + \sigma_{\text{rad}}^2)^{1/2}$ ). Such a radius is also small enough to avoid large numbers of chance associations.

Given  $r_{ij}$ , we must now distinguish between two conflicting possibilities: (1) that the candidate is a confusing background object which, by chance happens to lie at distance  $r_{ij}$  from the radio source, or, (2) that the candidate is the ‘true’ identification, which appears at distance  $r_{ij}$  purely due to radio and optical position uncertainties. We assume that the radio and optical positions would coincide if these uncertainties were zero. This assumption however is not valid when the centroid of an extended radio source is used, and is further discussed below.

To distinguish between these cases, we compute a statistic  $LR$ , defined as:

$$LR_{ij} = \frac{\exp[-r_{ij}^2/2]}{2\pi N(< m_i) \left[ (\sigma_{\alpha_i}^2 + \sigma_{\alpha_j}^2)(\sigma_{\delta_i}^2 + \sigma_{\delta_j}^2) \right]^{1/2}}, \quad (2)$$

where  $N(< m_i)$  is the *local* surface density of objects brighter than candidate  $i$ . The likelihood ratio  $LR_{ij}$  is simply the ratio of the probability of an identification (the Rayleigh distribution:  $r \exp(-r^2/2)$ ), and that of a chance association at  $r$  ( $2\pi N(< m_i)\sigma_{\alpha}\sigma_{\delta}$ ).  $LR_{ij}$

therefore represents a ‘relative weight’ for each match  $ij$ , and our aim is to find an optimum cutoff  $LR_c$  above which a source is taken to be a reliable and likely candidate. Its advantage over previous methods (purely based on finding the lowest random chance match) is that it allows for a possible distant candidate to still be the ‘true’ identification even when there is still a high chance of it being a spurious background source. The  $LR$  method is also insensitive to variations in  $N(< m_i)$  across the field or uncertainties in its derivation, and also the assumption of Gaussian error ellipses in the radio and optical positions. Lonsdale et al. (1998) have shown that the absolute value of  $LR$  itself depends on the characteristics of the source population being identified (eg. stars versus galaxies). To a high degree of certainty, it is likely that our radio sample comprises mainly galaxies with their own underlying optical surface density (regardless of morphological type).

The optical surface density as a function of magnitude to be used in computing  $LR$  was determined a-priori from the total number of objects visible in our optical frames. The variation in surface density in the local vicinity of each radio source from possible clustering effects was found to be small, varying by no more than 5% on  $2 - 3'$  scales.

The distribution of  $LR$  values for all possible radio source-candidate matches is shown by the shaded histogram in Figure 5. To generate a truly random background population with respect to the radio sources, the radio source positions were offset by  $\approx 30''$ .  $LR$  values for each radio source were then re-computed and their distribution is given by the thick-lined histogram in Figure 5. A comparison of the number of associations for (true) radio source positions with the number of associations found for random (offset) positions will enable us to determine a critical value  $LR_c$  for reliable identification. From these distributions, we compute the reliability as a function of  $LR$ :

$$R(LR_{ij}) = \frac{N_{true}(LR_{ij})}{N_{true}(LR_{ij}) + N_{random}(LR_{ij})}, \quad (3)$$

where  $N_{true}$  and  $N_{random}$  are the number of true and random associations respectively.

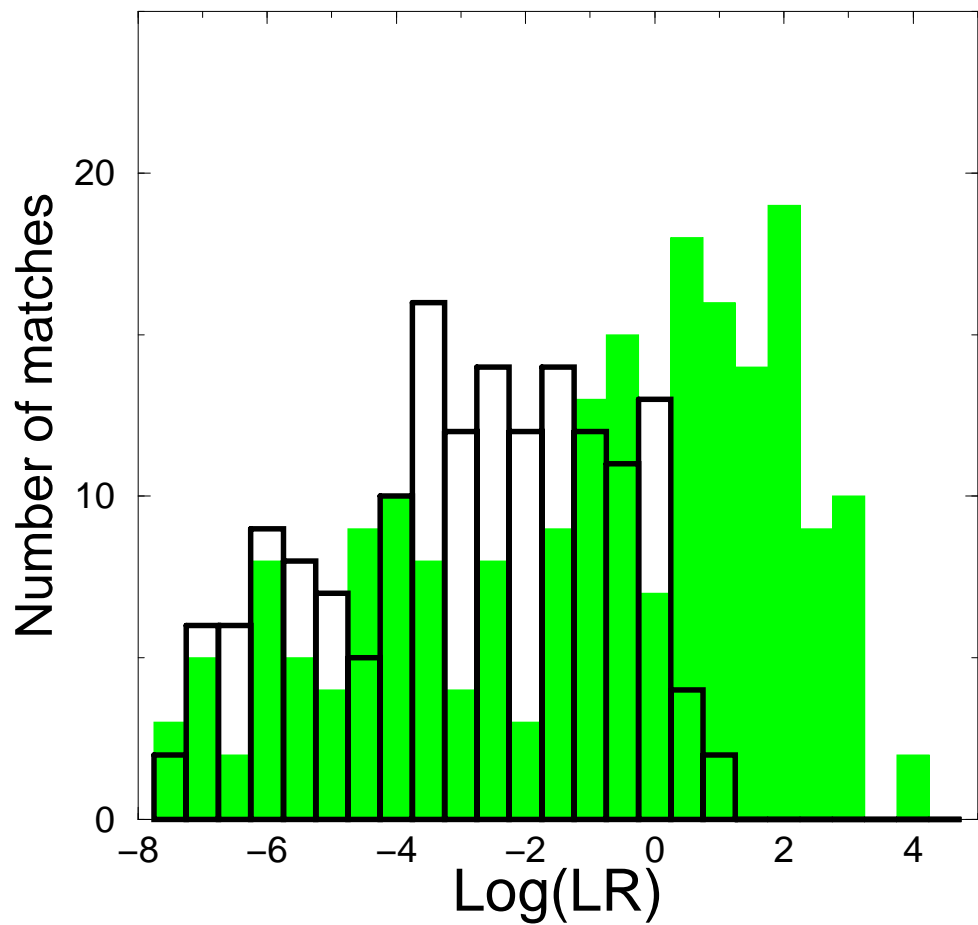


Fig. 5.— Distribution of  $LR$  for radio-optical matches at “true” radio positions (thick-lined histogram), and at “random” radio positions (shaded histogram).

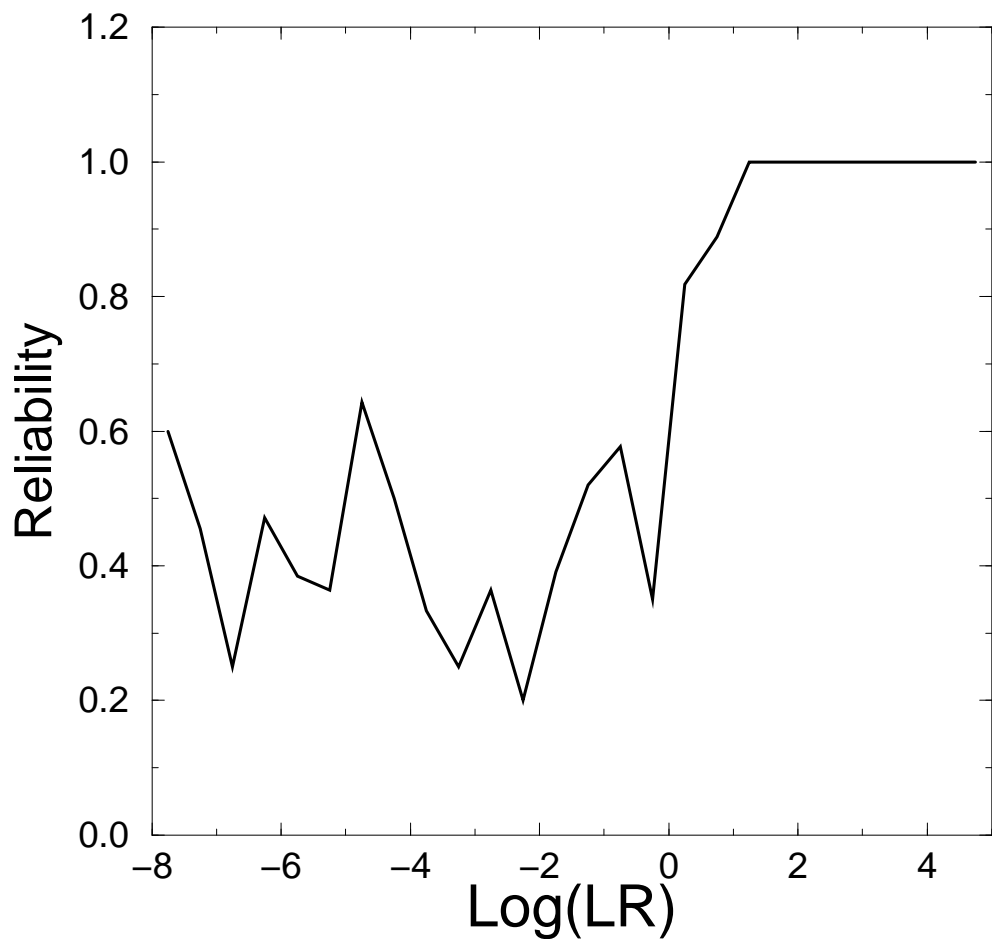


Fig. 6.— Reliability as a function of  $LR$ . See equation (3).

Figure 6 illustrates the reliability as a function of  $LR$ . Above  $\log(LR) \sim 0.5$ , the reliabilities are  $\gtrsim 85\%$  because few random associations exceed this value of  $LR$  (Fig. 5). As a good working measure we therefore assume a cutoff  $\log(LR_c) \simeq 0.5$  above which a source is taken to be a likely candidate. For each corresponding candidate with  $LR > LR_c$ , we also compute the probability that it is the “true” identification. For a homogenous population of sources (eg. galaxies, known a-priori), Prestage & Peacock (1983) show that the identification probability  $P_{id}$  depends on  $LR$  through the following upper and lower bound:

$$\left(1 - \frac{1}{LR(r_{ij})}\right) \leq P_{id}(r_{ij}) \leq \left(1 + \frac{1}{LR(r_{ij})}\right)^{-1}, \quad (4)$$

where  $P_{id}(r_{ij}) \approx 1 - 1/LR(r_{ij})$  for large  $LR(r_{ij})$ . It is important to note that using  $LR$  as a direct estimate of the identification probability strongly assumes that one is dealing with a uniform source population (cf. Lonsdale et al. 1998). Different populations (assuming they could be classified a-priori using some diagnostic) map into different underlying surface densities at the ‘identifying’ wavelength, implying that distributions in  $LR$  (eq. 2) will also be different.

There are two complications to consider in the above method. The first is when one attempts to identify extended (or resolved) radio sources with this method. For all radio sources, we have used the positions of centroids derived from two-dimensional Gaussian fits in computing the  $LR$  for optical candidates. For unresolved sources with sizes  $\lesssim 15''$  (the synthesised FWHP beam width), the source is likely to have a compact central component and the optical position is expected to lie close to its quoted radio centroid. For an extended (resolved) source however, the radio and optical positions may differ considerably since errors in the radio centroids are only  $\lesssim 2''$ . In such cases, if  $LR < LR_c$  the identification may still be valid, since its low  $LR$  value could purely be due to a large positional offset. The second complication is when a radio source has more than one optical candidate within its search radius with  $LR > LR_c$ . This occurred in about 20% of cases and was primarily

due to contaminating stars. We assess these ambiguities and increase the robustness of our identifications by visually examining all optical candidates according to the following criteria:

1. If candidates have  $LR < LR_c$  for a radio source with  $\theta_{min,max} \gtrsim 15''$ , then identification is classified as *uncertain*.
2. If  $LR \lesssim LR_c$ , i.e. where identification probabilities are moderately “low”, then identification is also uncertain.
3. If candidates have  $LR < LR_c$ , or there are no objects in the search radius, then radio source is classified as *empty field*.
4. If more than one optical candidate exists with  $LR > LR_c$ , then only source(s) with extended (galaxy-like) optical profile is taken as identification.
5. For unique,  $LR > LR_c$  candidates, its optical profile is also checked for confirmation.

## 4.2. Results

Out of the 62 radio sources, 43 were within our optically imaged  $27.5 \times 27.5 \text{ arcmin}^2$  field. Of these, we propose robust optical identifications for 26 to  $r \simeq 25$  mag with  $P_{id} \gtrsim 80\%$  and reliabilities  $\gtrsim 85\%$ . Four sources are classified as uncertain due to a moderately low identification probability of  $P_{id} \lesssim 67\%$  (and  $\log(LR) \lesssim 0.5$ ). Five are also uncertain due to extended radio structure and large possible positional offsets between optical and radio centroid positions. Eight sources were classified as “definite” optical empty fields with  $r > 25$  mag.

To compare this with the results of other optical follow-up studies, Georgakis et al. (1999) identified  $\approx 47\%$  of sources to  $R = 22.5$  mag from the Phoenix Deep Survey

( $S_{1.4\text{GHz}} > 0.2\text{mJy}$ ) (Hopkins et al. 1998). A deeper identification study of sources detected to  $S_{1.4\text{GHz}} \simeq 40\mu\text{Jy}$  from Hubble Deep Field images revealed a 80% success rate to  $I = 25\text{mag}$  (Richards et al. 1999). Ignoring the uncertain classifications in our study (which can be attributed to beamsize limitations), we find that  $\approx 18\%$  are unidentified to  $r \sim 25$ . Accounting for differences in bandpasses and sensitivity, this is broadly consistent with the above studies. Figure 7 shows the distribution of apparent magnitude  $r$  for all reliable (robust) and uncertain identifications in our sample.

Near-infrared data in the  $J(1.25\mu\text{m})$ ,  $H(1.65\mu\text{m})$  and  $K_s(2.17\mu\text{m})$  photometric bandpasses was obtained from the Two Micron All Sky Survey (*2MASS*) project database. For multi-band detection of point sources, this survey is currently scanning the sky to sensitivities 16.5, 16.0 and 15.5 mag at signal-to-noise ratios  $\approx 7$ ,  $\approx 5$  and  $\approx 7$  respectively in  $J$ ,  $H$  and  $K_s$ . A large portion of the completed survey is not yet available for public use, which includes the data relevant to this study. The data was thus retrieved from the ‘internal working database’ at *IPAC*<sup>6</sup> (Cong Xu; private communication). Photometric fluxes in this database are primarily “default” magnitudes from point spread function (PSF) fitting using the **DAOPHOT** source extraction package. All magnitudes were aperture corrected using standard calibrators.

We searched for near-infrared candidates to each radio source regardless of their photometric uncertainty from the PSF fit, which we also quote (see Table 3). In cases where a source was detected in only one or two of the three bandpasses –  $J$ ,  $H$  and  $K_s$ , we note its “band-filled” 95% confidence upper-limit in the undetected band. The image pixel scale of the *2MASS* detectors is  $2.0''$  and positional uncertainties  $\lesssim 0.5''$ . Due to the relatively shallow flux limits of the *2MASS* survey, the source surface density was low enough that chance-associations could be neglected to a high degree of confidence.

---

<sup>6</sup>The Infrared Processing and Analysis Center, California Institute of Technology.

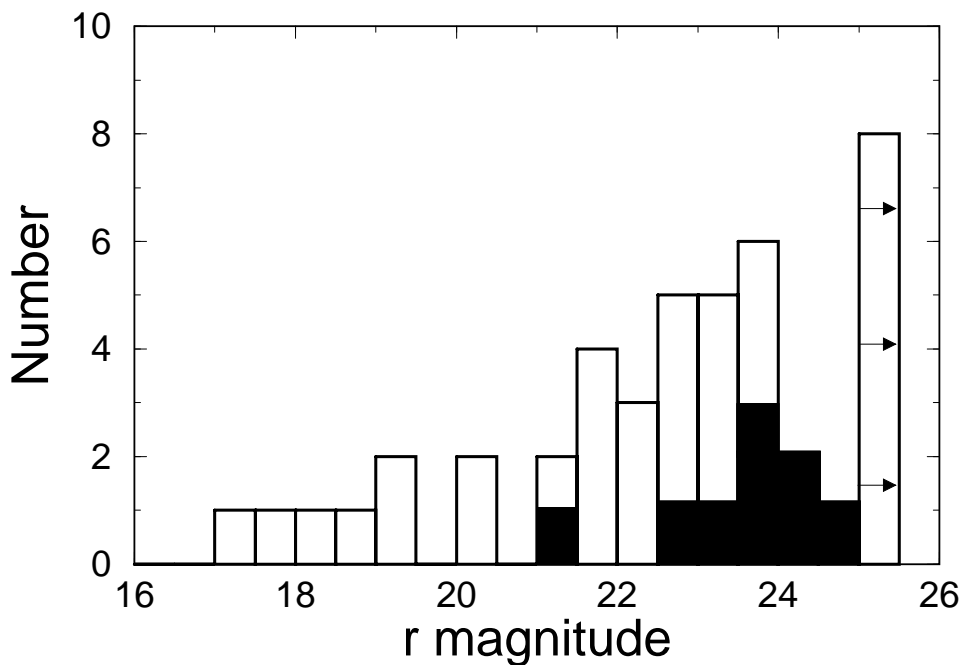


Fig. 7.— The distribution of apparent  $r$ -band magnitudes for the 26 identified radio sources (open histogram) and nine uncertain identifications (filled histogram). Eight empty fields are represented by the  $r > 25$  magnitude bin with arrows.

A search in the *2MASS* catalog for near-infrared counterparts to our 43 radio sources with *available optical* information found 11 photometric measurements. For each band respectively, we have 4 detections in  $J$ , 8 in  $H$ , 3 in  $K_s$  and upper limits for the remaining “band-filled” values.

Results of our optical identification analysis and available near-infrared data is shown in Table 3. In column order, this table reports: the radio source name (see Table 2); RA and Dec.(J2000) of the optical counterpart of the radio source; optical-radio position separation ( $\delta_{rad-opt}$ ) in arcsec; logarithm of the likelihood ratio ( $LR$ ); probability that the optical candidate is the “true” identification (see eq.[4]); apparent  $r$ -band magnitude;  $J$ ,  $H$  and  $K_s$  magnitudes with errors or  $2\sigma$  upper limits;  $r - H$  color;  $r - K_s$  color, and last, the optical morphology if the optical counterpart is visually resolved.

### 4.3. Optical and Radio Map Overlays

In Figure 8 we show the optical image – radio map overlays for the 43 radio sources with available optical information. A visual inspection of the optical images of resolved counterparts shows a diverse morphological mix, consistent with previous studies. About 40% of our optical identifications have elliptical/disk-like morphology, while  $\sim 10\%$  can be identified as exhibiting peculiar (either compact, interacting and irregular) morphologies.

Fig. 8.— Available at <http://spider.ipac.caltech.edu/staff/fmasci/papers/> (click on “Figure8.ps”). Optical image ( $r$ -band) and radio contour overlays for the 43 sources with available optical information. Contour levels are  $1\sigma$ ,  $2\sigma$ ,  $3\sigma$ ,  $4\sigma$ ,  $5\sigma$ ,  $10\sigma$ ,  $20\sigma$ ,  $30\sigma$ ,  $40\sigma$ ,  $50\sigma$ ,  $100\sigma$  and  $200\sigma$ , where  $\sigma$  refers to the local rms noise (see Table 1).

The elliptical/disk hosts also tend to be associated on average with sources of relatively brighter radio flux density ( $\gtrsim 2$  mJy) than the irregular class. This is consistent with previous radio-optical identification studies which find an increasing fraction of irregular-type galaxies at  $S_{1.4} \lesssim 2$  mJy (eg. Kron, Koo & Windhorst 1985, Hammer et al. 1995, Gruppioni et al. 1998), and, a significant number of elliptical hosts contributing at brighter fluxes, namely the classical extended radio galaxies and AGN (Condon 1989).

A further observation is the unique radio structure exhibited by our optical empty field sources at  $r > 25$  mag. All show compact and symmetric (presumably unresolved) structures and could represent either of the following: distant (possibly dusty) AGN where with our radio sensitivity, we could have detected a nominal FR-I galaxy to  $z \sim 1.3$ , or, nearby, compact dusty starbursts at  $z \lesssim 0.3$ . The second explanation for the nature of the empty fields is more plausible, given that the majority of submillijansky radio sources are associated with star-forming galaxies and less than 5% are usually identified with bright FR-Is at  $z \lesssim 1$  (Kron, Koo & Windhorst 1985).

## 5. ANALYSIS OF RADIO AND OPTICAL-NEAR-INFRARED COLORS

This section presents an analysis of flux ratios between the radio, near-infrared and optical bands to explore possible contributions from AGN and starbursts to the observed radio emission, as well as the importance of extinction by dust. Despite the lack of spectroscopic information, our analysis will treat the sub-mJy sources as one homogeneous population and use a simple stellar synthesis model to qualitatively interpret its properties.

### 5.1. A Simple Synthesis Model

We predict the radio-to-optical(-near-IR) flux ratios and  $r - K$  colors for a range of galaxy types using the stellar population synthesis code of Bruzual & Charlot (1993) (hereafter BC). On its own however, the BC model does not directly predict the amount of radio emission expected from a star-forming galaxy, which we need for the determination of flux ratios involving the radio band. We do this by relating the star formation rates derived from empirical calibrations involving the UV and radio bands as follows.

The 1.4 GHz radio emission from star-forming systems is believed to be primarily synchrotron emission from supernova remnants with a small ( $\lesssim 10\%$ ) thermal contribution from HII regions (Condon & Yin 1990, Condon 1992). Thus to a good approximation, the radio luminosity is taken to be proportional to the formation rate of high-mass stars with typically  $M > 5M_{\odot}$  which produce supernova:

$$SFR(M \geq 5M_{\odot}) = \frac{L_{1.4\text{GHz}}}{4 \times 10^{28}\text{ergs}^{-1}\text{Hz}^{-1}} M_{\odot}\text{yr}^{-1}. \quad (5)$$

(Condon 1992). These same massive stars will also contribute significantly to the UV continuum emission in the range  $\sim 1200\text{-}2500\text{\AA}$ . In particular, there have been many different calibrations of the SFR from the UV-flux. For a Salpeter initial mass function (IMF) from 0.1 to  $100M_{\odot}$ , the calibration of Madau et al. (1998) yields

$$SFR(M \geq 0.1M_{\odot}) = Q_m \left( \frac{L_{UV}}{7.14 \times 10^{27}\text{ergs}^{-1}\text{Hz}^{-1}} \right) M_{\odot}\text{yr}^{-1}. \quad (6)$$

We have modified the initial relation of Madau et al. (1998) to include the factor  $Q_m$ , which represents the fraction of stellar masses contributing to the observed SFR,

$$Q_m = \frac{\int_m^{100M_{\odot}} M\psi(M)dM}{\int_{0.1M_{\odot}}^{100M_{\odot}} M\psi(M)dM}, \quad (7)$$

where  $\psi(M) \propto M^{-x}$  is the IMF. For  $m = 0.1$ , we have  $Q_m = 1$ . Assuming a Salpeter IMF ( $x = 2.35$ ), we find that for massive supernova producing stars with  $M > 5M_{\odot}$ ,  $Q_m \simeq 0.18$ .

With this fraction, and equating the two SFR calibrations (eqs [5] and [6]), we find that the luminosity densities at 1.4 GHz ( $L_{1.4GHz}$ ) and  $\simeq 2100\text{\AA}$  ( $L_{UV}$ ) are very nearly equal. We therefore assume that the rest frame 1.4 GHz flux density is directly given by the flux density at  $\simeq 2100\text{\AA}$  as specified by the synthesised model spectrum. In general terms, the observed radio flux (in arbitrary units of the synthesised UV spectrum), can be written:

$$f_\nu(1.4\text{GHz})_{obs} = (1+z)^{1-\alpha} f_\nu(2100\text{\AA})_{int}, \quad (8)$$

where  $\alpha \simeq 0.8$  is the radio spectral index (Condon 1992) and  $f_\nu(2100\text{\AA})_{int}$  is the intrinsic UV spectral flux. We must emphasise that this relative radio flux is only that associated with the star formation process. Possible additional contributions, such as contaminating AGN will not be considered here.

The flux ratios involving the radio, near-infrared and optical bands are generated using evolutionary synthesis models for ellipticals (E/SO), early (Sab/Sbc) and late (Scd/Sdm) type spirals and “very blue” starbursts (SB). These are meant to represent the possible contributions to the sub-mJy radio sources and each class is defined by a characteristic star formation rate as a function of time. As supported by local observations, we assume that E/SO and Sab/Sbc galaxies have an exponentially decaying SFR of the form  $\psi(t) \propto \tau^{-1} \exp(-t/\tau)$ , where  $\tau$  is the e-folding time. Values of  $\tau = 1$  and  $\tau = 8$  Gyr are adopted for the E/SO and Sab/Sbc galaxies respectively. For late type spirals (Scd/Sdm) and young starbursts (SB), we assume a constant SFR with different ages. All models used to generate the spectral energy distributions (SEDs) are summarised in Table 4. The models assume  $H_0 = 50 \text{ km s}^{-1} \text{ Mpc}^{-1}$ ,  $q_0 = 0.5$  and a galaxy formation redshift of  $z_f = 10$ , which corresponds to an age of 12.7 Gyr at  $z = 0$ .

To explore the effects of dust on our flux ratios and colors, each model SED is reddened intrinsically using an extinction curve  $\xi(\lambda) \equiv A_\lambda/A_V$  characteristic of the Small Magellanic Cloud. We have used an analytical fit for  $\xi(\lambda)$  as derived by Pei (1992). For simplicity, we

assume the dust is distributed in a homogeneous foreground screen at the source redshift.

## 5.2. Data and Model Comparisons

In Figure 9 we plot the radio-to-optical flux ratio,  $R(1.4/r)$ , defined as

$$R(1.4/r) = \log (S_{1.4}/\text{mJy}) + 0.4 r, \quad (9)$$

where  $S_{1.4}$  and  $r$  are the radio flux and optical  $r$ -band magnitude respectively. The scatter in  $R(1.4/r)$  appears relatively large at the faintest optical magnitudes  $r > 22$ . The statistics at  $r < 21$  however are very low, and nonetheless, such scatter is consistent with that found at  $r \lesssim 19$  in a larger follow-up study of sub-mJy radio sources by Georgakakis et al. (1999).

Figure 10 shows  $R(1.4/r)$  as a function of  $r - H$  color for all sources with available optical and near-infrared data. Our reason for using  $r - H$  color is that the  $H$  band contains the most number of ‘robust’ detections than the other near-infrared bandpasses. Although the statistics are still relatively small, this facilitates the best comparison with the synthesis models. The predictions for four galaxy types (see Table 4) are shown for no dust reddening (thin curves), and, assuming a rest frame extinction  $A_V = 2.5$  mag. The morphological mix of data shows a relatively large dispersion in  $r - H$  color that is more consistent with the range predicted by the models that *include dust*. This suggests that on average, the optical-to-near-infrared continua of most sources in Fig. 10 are reddened by an “optically-thin” dust component with  $A_V \simeq 2 - 2.5$  mag extinction. This measure is consistent with spectroscopic studies of nearby starbursts by Calzetti et al. (1996), Meurer et al. (1997) and photometric modelling by Nakata et al. (1999).

The sources in Fig. 10 appear more-or-less consistent with the dusty “0.1 Gyr starburst” model. This could in principle apply to the three sources with spiral/disk-like morphology (labelled “S”), but is unconventional for the five elliptical (presumably early-type)

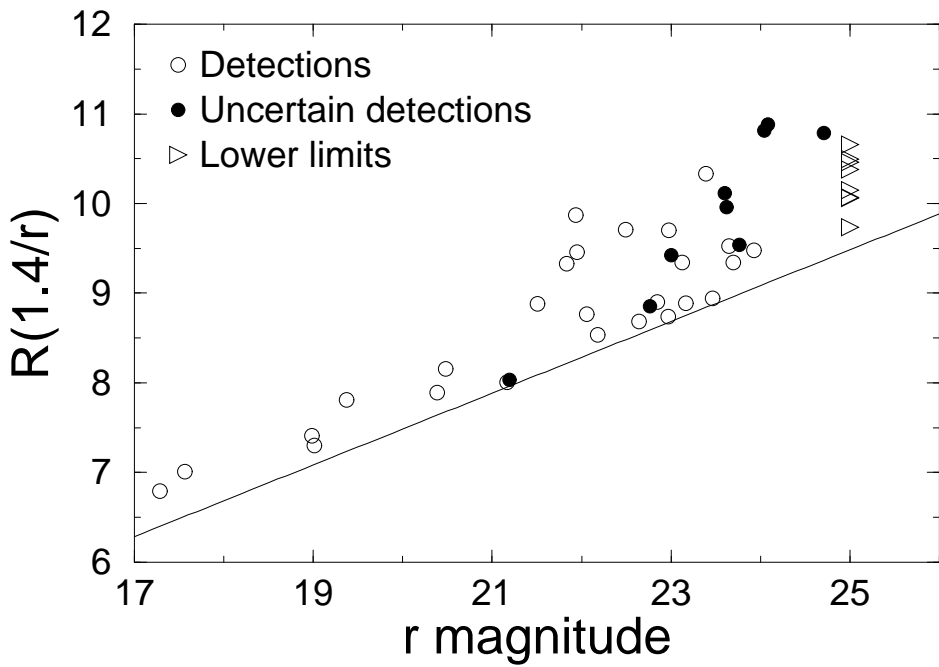


Fig. 9.— Radio-to-optical ( $r$ -band) flux ratio (see eq.[ 9]) as a function of  $r$  magnitude for all radio sources with available optical information. The solid line represents the prediction at the limiting flux of the survey  $S_{1.4\text{GHz}} \approx 0.3\text{mJy}$ .

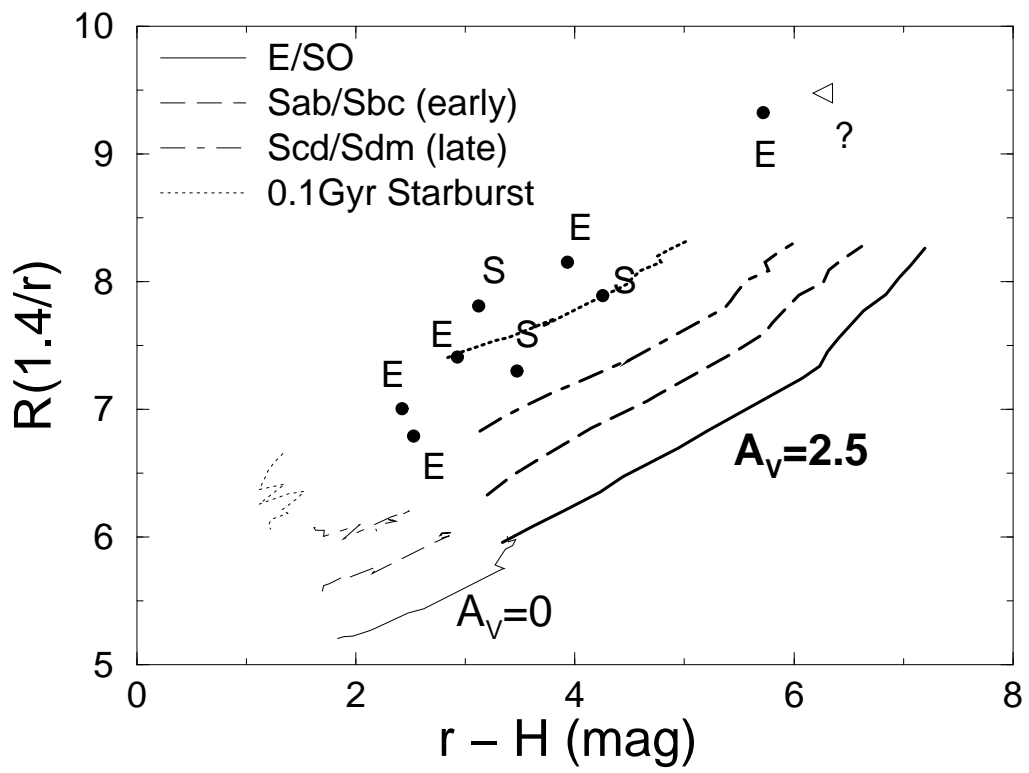


Fig. 10.— Radio-to-optical ( $r$ -band) flux ratio (see eq.[ 9]) as a function of  $r - H$  color for radio sources with available optical and near-infrared detections. The triangle represents an upper limit on  $r - H$ . The predictions of four synthesis models for  $0 \leq z \leq 1.5$  ( $z = 0$ —starting bottom left of curves to  $z = 1.5$ —top right) are also shown. These assume (a) no extinction (thin curves) and (b) with a rest-frame extinction  $A_V = 2.5$  mag (thick curves).

morphologies. A comparison with radio-to-near-infrared flux ratios further constrains the underlying properties of these sources. Figure 11 shows the radio-to-near-infrared flux ratio  $R(1.4/H)$ , defined analogous to eq.[9] as a function of  $r - H$  color. The near-infrared emission is dominated by old stars, and is less affected by dust than the optical. The radio-to-near-infrared flux ratio should therefore be relatively insensitive to dust. Given their simplicity, the models do not exclude the possibility that the three disk-like sources could belong to the Sab/Sbc or Scd/Sdm classes. This will require either of the following additional components to our models: ‘optically-thick’ dust that *completely obscures* both the  $H$  and  $r$  emission without causing appreciable reddening in  $r - H$  color, or, contamination by at least an order of magnitude times more radio emission from a central AGN than that produced purely by supernovae. The second possibility is favored by observations of a number of Seyfert nuclei associated with spiral hosts (eg. Norris et al. 1988).

The large discrepancy between the five sources with elliptical morphologies (labelled “E”) and predictions from the early-type E/SO models suggests the importance of a significant AGN contribution to the radio emission. Appreciable amounts of optically-thick dust suppressing the optical-to-near-infrared light (except for extinction by diffuse, optically-thin dust) is not favored by observations (eg. Goudfrooij & de Jong 1995). Most, if not all of these ellipticals are likely to be radio-powered by AGN, similar to the classical FR-I/FR-II radio morphologies. At the limiting sensitivity of our radio survey ( $\simeq 0.3$  mJy), a nominal FR-I galaxy (with  $L_{1.4} = 10^{24} \text{ W Hz}^{-1}$ ) could be detected to  $z \simeq 1.3$ , and indeed the spread in  $r - H$  color for the ellipticals in Fig. 11 is consistent with the E/SO (optically-thin dust) model to this redshift. A comparison between the model  $R(1.4/H)$  values with actual observed values implies that such AGN will contribute a factor  $10^2$  times more radio emission than that produced by any underlying star formation activity in these systems.

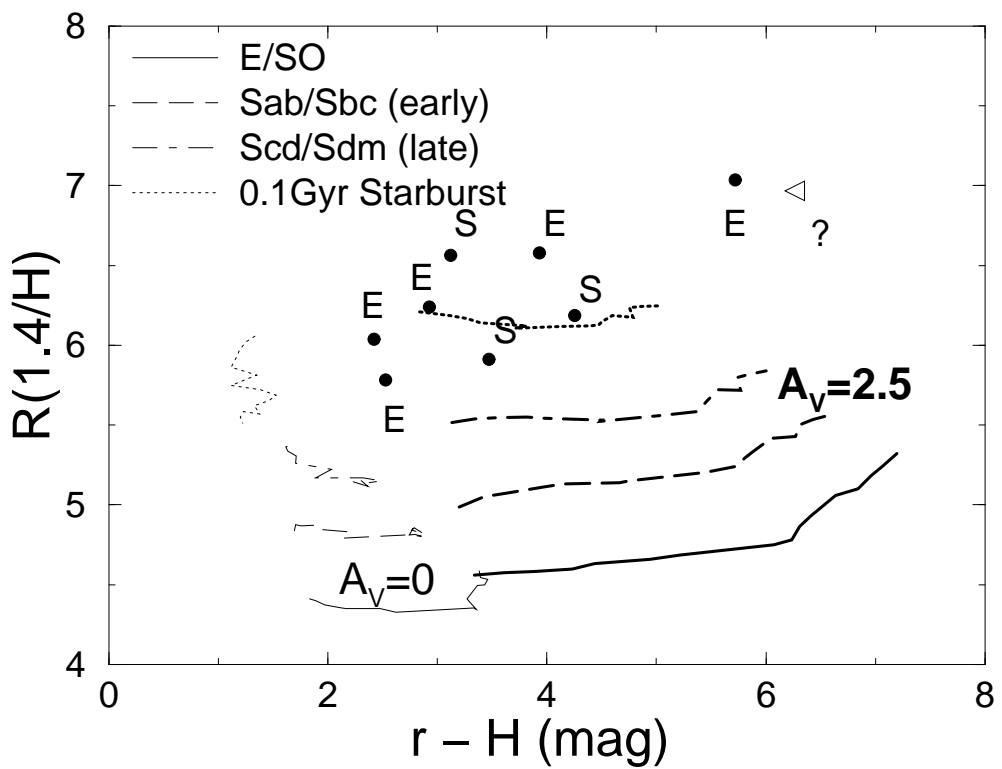


Fig. 11.— Radio-to-near-infrared ( $H$ -band) flux ratio as a function of  $r - H$  color and models which include (a) no extinction and (b)  $A_V = 2.5$  mag, similar to Fig. 10. The source labelled as a triangle is both an upper limit on  $r - H$  and, a lower limit on  $R(1.4/H)$ .

To summarise, our use of a simple synthesis model that includes radio emission and dust reddening to analyse the properties of sub-mJy radio sources has shown the following: first, the presence of dust with extinctions  $A_V \simeq 2$  mag and possibly greater consistent with previous more direct determinations, and second, that radio emission from non-stellar precesses such as AGN could be easily inferred and constrained.

## 6. A Method to Select “ULIGS” via Radio/Optical Color

Since the emission (and dust absorption) properties from normal galaxy populations are reasonably well known, a color-color diagram such as Fig. 10 could provide a potential diagnostic for selecting ultraluminous infrared galaxies (ULIGS) to high redshift. The relatively low sensitivity of the Infrared-Astronomical Satellite (IRAS) has primarily confined ULIG selection to the local Universe (Sanders & Mirabel 1996), although there is some speculation that recently discovered faint “SCUBA” sources at sub-millimetre wavelengths could represent their high-redshift counterparts (eg. Blain et al. 1999). Approximately 80% of local ULIGS are believed to be powered by starbursts and the remainder show evidence for an AGN contribution (Genzel et al. 1998; Lutz et al. 1998). Far-infrared observations have shown that dust and molecular gas in local ULIGS is concentrated in compact regions  $\lesssim 1\text{kpc}$  (eg. Scoville et al. 1991) and that a large fraction of the stellar optical/UV emission is hidden by “optically-thick” dust. A study of their properties and importance to studies of galaxy evolution therefore requires observations at wavelengths virtually immune to dust absorption. The radio provides an excellent window of opportunity.

Figure 12 illustrates the predicted locus in color-color space using the synthetic SEDs of three local far-IR selected systems: Arp 220 ( $L_{IR} \simeq 1.6 \times 10^{12} L_\odot$ ) - a ULIG undergoing a powerful starburst as seen via high resolution radio observations by Smith et al. (1998a);

M82 ( $L_{IR} \simeq 6 \times 10^{10} L_{\odot}$ ) - a system undergoing a weak-to-moderate starburst, and Mrk 273 ( $L_{IR} \simeq 2.6 \times 10^{12} L_{\odot}$ ) - a ULIG whose bolometric emission is believed to be dominated by a hidden central AGN from the presence of broad Seyfert-1 lines and faint symmetric radio jets (Smith et al. 1998b). We have used synthetic SEDs generated by Devriendt et al. (1999). These authors used a self-consistent modelling approach to predict the stellar optical/UV/near-IR emission, its reprocessing into the mid-IR-to-sub-mm by dust, and the non-thermal stellar induced radio emission using the empirical radio-to-far-IR luminosity correlation. Due to its strong AGN-dominated nature, we did not use the *radio* SED for Mrk 273 as predicted by Devriendt et al. Instead, we used the Devriendt et al. SED at wavelengths  $\lambda < 1\text{mm}$  and extrapolated into the radio using its observed radio-to-1mm spectral slope and fluxes (obtained from the NASA/IPAC Extragalactic Database<sup>7</sup>).

Figure 12 shows that a galaxy characteristic of the (low-IR luminous) M82 system will occupy a region similar to that occupied by normal galaxies in this study (and also their predicted synthetic colors in Fig. 10). Luminous systems classified as ULIGS however (Arp 220 and Mrk 273), will tend have redder radio-to-optical flux ratios that could be easily selected. This can be explained by the well-observed correlation between far-infrared luminosity and far-IR ( $60 - 100\mu\text{m}$ )-to-optical spectral slope (Sanders & Mirabel 1996 and references therein). Consequently, the most IR-luminous systems with the largest far-IR-to-optical ratios are also likely to have a high level of radio-emission due to its strong correlation with IR luminosity. This will lead to a larger than average radio-to-optical flux ratio for ULIGS in general as shown in Fig. 12.

The existence of systems with either larger rest-frame optical/UV extinction or

---

<sup>7</sup>The NASA/IPAC Extragalactic Database (NED) is operated by the Jet Propulsion Laboratory, California Institute of Technology, under contract with the National Aeronautics and Space Administration.

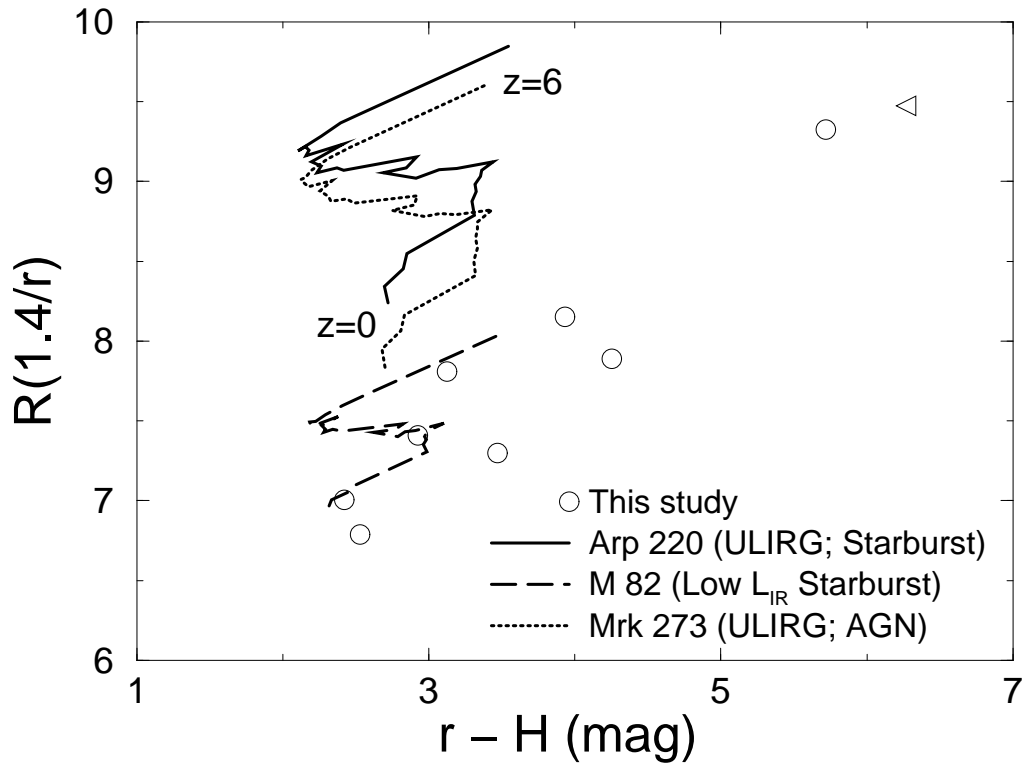


Fig. 12.— Locus of radio-to-optical flux ratio versus  $r - H$  color for  $0 \leq z \leq 6$  ( $\Delta z = 0.2$ ) using three local far-IR selected systems: Arp 220 ( $L_{IR} \simeq 1.6 \times 10^{12} L_{\odot}$ ; strong starburst), M82 ( $L_{IR} \simeq 6 \times 10^{10} L_{\odot}$ ; weak/moderate starburst) and Mrk 273 ( $L_{IR} \simeq 2.6 \times 10^{12} L_{\odot}$ ; AGN dominated).

excess AGN contribution to the radio than the ULIGS considered here will be shifted further upwards on this plot. A system like Arp 220 (with  $L_\nu(1.4\text{GHz}) \simeq 2.5 \times 10^6 L_\odot$ ) could be observed to redshift  $z \sim 1.6$ <sup>8</sup> if initially selected from a radio survey limited to  $S_{1.4\text{GHz}} \simeq 50\mu\text{Jy}$ . Thus, to limiting sensitivities reached by existing 1.4 GHz surveys, such a method may not probe the highest redshifts. Nonetheless, as shown in Fig. 12, such systems could still be well separated from normal galaxies to this redshift. Assuming an Arp 220-like SED and moderate luminosity evolution ( $L_{60\mu\text{m}} \propto (1+z)^{2.5}$ ), the surface density of ULIGS to  $z \sim 1.6$  is expected to be of order  $150 \text{ deg}^{-2}$  at  $S_{1.4\text{GHz}} \gtrsim 50\mu\text{Jy}$ , or about 6% of the integral count to this sensitivity (Richards 2000). They should therefore exist in significant numbers in deep, large area radio surveys.

## 7. SUMMARY AND CONCLUSIONS

We have used the VLA radio telescope to image a contiguous  $33 \times 33 \text{ arcmin}^2$  area to a (mean) limiting ( $5\sigma$ ) sensitivity of  $\simeq 0.34 \text{ mJy}$ . From a total of 62 detections, the results of optical and near-infrared photometry are reported for 43 sources. Our main findings are:

- (1) We have used a robust, likelihood-ratio method for determining optical identifications and their reliability. This method is seldom used in identification studies and is insensitive to assumptions concerning fluctuations in background source density and Gaussian error distributions. We assigned optical candidates to 26 radio sources with  $P_{id} \gtrsim 80\%$ . Nine radio sources are uncertain and/or ambiguous, and eight are empty fields. Near-infrared photometry from the *2MASS* database was reported for 11 sources.
- (2) The eight optical empty field sources all display compact and symmetric radio morphologies and most probably represent compact starbursts at  $z \lesssim 0.3$  strongly obscured

---

<sup>8</sup> Assumes  $q_0 = 0.5$ ,  $H_0 = 65 \text{ km s}^{-1} \text{ Mpc}^{-1}$

by dust.

(3) Consistent with previous studies, our deep ( $r \simeq 25$ ) optical imaging shows that the optical appearance can be divided into two classes according to radio flux-density: elliptical-like morphologies for  $\gtrsim 2$  mJy, and peculiar or disturbed for  $\lesssim 2$  mJy.

(4) Using a stellar synthesis model which includes radio emission and dust reddening, we find that the near-infrared-to-optical emission in a small, bright sub-sample is reddened by ‘optically thin’ dust with  $A_V \simeq 2 - 2.5$  mag, regardless of morphological type. This appears consistent with other more direct determinations. Early-type systems in particular require significant contamination in the radio from an AGN to account for their anomalously large radio-to-optical(–near-infrared) ratios.

(5) Our analysis shows that a radio/optical or radio/near-IR color selection technique could provide a potential means for detecting ubiquitous ULIG-type objects to  $z \sim 1.6$ .

Despite the lack of spectroscopic information, our study of a homogeneous population of faint radio sources has stressed the importance of dust on studies of intrinsic galaxy properties and their evolution at optical wavelengths. The ever increasing resolution (and sensitivity) capabilities of optical/near-IR detectors over those feasible at (the longest) radio wavelengths requires robust identification techniques to better ascertain their properties. The “likelihood-ratio method” provides one such technique. The present study complements other deep optical studies of faint radio sources to constitute a statistically significant sample for inferring their nature and importance to observational cosmology.

FJM thanks Glenn Morrison and JoAnn O’Linger for valuable assistance with the data reduction and Cong Xu for providing the archival *2MASS* data. We thank the staff at Palomar Observatory for technical assistance during the observing run. The *2MASS* database is maintained by IPAC/JPL and supported by NASA. The *NVSS* catalog is

maintained by the National Radio Astronomy Observatory and funded by the National Science Foundation. This reasearch has made use of the NASA/IPAC extragalactic database (NED) which is operated by the jet propulsion laboratory, caltech, under contract with the national aeronautics and space administration. FJM acknowledges support from a JPL/NASA postdoctoral fellowship grant.

Table 1. The regions used for the source extractions

Region	RA(J2000) <sup>a</sup>	Dec(J2000) <sup>a</sup>	$\sigma_{rms}$	$5\sigma$ limit	# sources <sup>b</sup>
			(mJy)	(mJy)	
1	00 <sup>h</sup> 13 <sup>m</sup> 48 <sup>s</sup> .43	+25°48'07".7	0.061	0.305	15
2	00 <sup>h</sup> 12 <sup>m</sup> 34 <sup>s</sup> .09	+25°47'11".7	0.065	0.325	15
3	00 <sup>h</sup> 12 <sup>m</sup> 33 <sup>s</sup> .11	+26°03'27".7	0.090	0.450	20
4	00 <sup>h</sup> 13 <sup>m</sup> 48 <sup>s</sup> .21	+26°02'47".7	0.076	0.380	14 <sup>c</sup>

<sup>a</sup>Defines the center of each region with size  $\approx 16.5 \times 16.5$  arcmin<sup>2</sup>.

<sup>b</sup>Total number of sources with flux density  $\geq 5\sigma_{rms}$ .

<sup>c</sup>Includes the separate components of two double-component sources.

TABLE 2  
CATALOG OF RADIO SOURCE DATA

Name	RA(J2000) (h, m, s)	Dec(J2000) ( $^{\circ}$ $'$ $''$ )	$\sigma_{RA}$ ( $''$ )	$\sigma_{Dec}$ ( $''$ )	$S_P$ (mJy)	$\sigma_{S_P}$ (mJy)	$S_T$ (mJy)	$\sigma_{S_T}$ (mJy)	$\theta_M$ ( $''$ )	$\theta_m$ ( $''$ )	PA (deg)	$\sigma_{\theta_M}$ ( $''$ )	$\sigma_{\theta_m}$ ( $''$ )	$\sigma_{PA}$ (deg)
RADJ001158+2550	00 11 58.0587	+25 50 24.41	0.374	0.434	1.468000	0.095	1.410000	0.088	15.944	13.579	169	1.027	0.875	16
RADJ001158+2556	00 11 58.0787	+25 56 48.20	0.244	0.263	2.176000	0.095	2.820000	0.075	14.482	12.969	24	0.630	0.564	16
RADJ001203+2544	00 12 03.9771	+25 44 54.18	1.356	1.063	0.424090	0.084	0.284790	0.116	15.249	9.908	63	3.402	2.210	20
RADJ001204+2540	00 12 04.3139	+25 40 37.21	0.227	0.219	2.653000	0.092	2.930000	0.118	15.797	13.559	51	0.563	0.484	9
RADJ001204+2605	00 12 04.5721	+26 05 01.42	0.668	0.619	0.973096	0.084	0.962700	0.036	18.466	12.055	129	1.795	1.172	9
RADJ001206+2611	00 12 06.1784	+26 11 05.20	0.495	0.591	1.096000	0.095	1.050000	0.046	16.439	13.115	19	1.419	1.132	15
RADJ001209+2540	00 12 09.6149	+25 40 24.41	0.308	0.317	1.880000	0.093	2.780000	0.099	14.993	14.237	29	0.755	0.717	39
RADJ001210+2551	00 12 10.3819	+25 51 36.54	0.400	0.437	1.402000	0.094	1.300000	0.110	16.091	12.989	147	1.086	0.876	13
RADJ001216+2601	00 12 16.0418	+26 01 31.64	0.035	0.038	17.676001	0.064	18.42000	0.108	17.051	15.245	10	0.091	0.081	2
RADJ001216+2543	00 12 16.8546	+25 43 02.09	0.609	0.571	0.955994	0.084	0.836040	0.140	14.521	13.550	100	1.437	1.341	58
RADJ001217+2602	00 12 17.1770	+26 02 53.96	0.733	0.619	0.878036	0.044	0.844680	0.159	16.079	13.462	99	1.732	1.450	24
RADJ001218+2554	00 12 18.0569	+25 54 44.99	0.133	0.133	4.580000	0.095	4.700000	0.173	15.301	15.081	47	0.316	0.311	18
RADJ001218+2539	00 12 18.1936	+25 39 42.82	0.070	0.071	8.443000	0.095	8.280000	0.167	14.927	14.783	16	0.167	0.166	17
RADJ001227+2543	00 12 27.1842	+25 43 39.10	3.098	3.679	0.240284	0.090	0.408250	0.207	26.143	14.623	144	9.884	5.529	25
RADJ001230+2610	00 12 30.1238	+26 10 40.53	1.385	1.352	0.716138	0.098	0.141035	0.201	33.900	13.072	134	4.253	1.640	5
RADJ001237+2607	00 12 37.2540	+26 07 48.87	0.547	0.534	1.157000	0.089	1.230000	0.147	16.823	14.221	49	1.375	1.163	20
RADJ001240+2609	00 12 40.3944	+26 09 57.71	1.182	1.578	0.447156	0.094	0.419860	0.157	18.876	11.192	153	3.994	2.368	16
RADJ001241+2610	00 12 41.0070	+26 10 31.16	0.316	0.285	2.006000	0.071	1.970000	0.116	16.611	13.268	121	0.783	0.626	8
RADJ001242+2600	00 12 42.2090	+26 00 33.55	0.188	0.182	3.229000	0.095	4.160000	0.086	15.278	14.392	62	0.448	0.422	20
RADJ001243+2558	00 12 43.3231	+25 58 10.05	0.519	0.508	1.158000	0.095	1.130000	0.136	15.394	14.207	52	1.257	1.160	41
RADJ001246+2543	00 12 46.0302	+25 43 51.08	2.248	1.636	0.344852	0.093	0.410820	0.123	19.944	13.441	107	5.430	3.659	17
RADJ001247+2602	00 12 47.6804	+26 02 38.49	0.864	0.907	0.559530	0.094	0.377550	0.127	12.744	11.914	21	2.155	2.014	12
RADJ001250+2550	00 12 50.0363	+25 50 10.68	0.451	0.461	1.224000	0.095	1.050000	0.151	14.153	13.629	26	1.094	1.054	83
RADJ001252+2549	00 12 52.0066	+25 49 38.49	1.218	1.880	0.655489	0.033	0.855640	0.130	20.303	14.466	82	2.881	2.053	17
RADJ001254+2600	00 12 54.8357	+26 00 48.52	0.347	0.344	1.656000	0.095	1.490000	0.125	14.504	13.978	130	0.829	0.799	63
RADJ001255+2541	00 12 55.3650	+25 41 53.48	0.149	0.126	4.717000	0.094	5.470000	0.182	17.566	14.852	96	0.351	0.296	5
RADJ001257+2559	00 12 57.2885	+25 59 43.59	0.849	1.334	0.544656	0.093	0.553990	0.155	18.083	11.514	179	3.141	2.000	15
RADJ001259+2607	00 12 59.1070	+26 07 18.91	1.867	1.445	0.497741	0.089	0.101946	0.218	24.476	18.828	84	4.406	3.390	27
RADJ001300+2556	00 13 00.9836	+25 56 57.10	0.183	0.181	3.230000	0.095	4.070000	0.096	15.100	14.147	129	0.442	0.414	18
RADJ001303+2602	00 13 03.1854	+26 02 07.41	0.119	0.118	5.136000	0.095	5.270000	0.097	15.289	15.108	112	0.282	0.278	23
RADJ001304+2544	00 13 04.0178	+25 44 25.38	0.891	0.968	0.545197	0.094	0.977020	0.129	13.924	11.175	146	2.416	1.939	32
RADJ001305+2607	00 13 05.3974	+26 07 54.15	0.189	0.160	3.906000	0.093	4.990000	0.119	19.377	14.842	115	0.462	0.354	4
RADJ001307+2542	00 13 07.0946	+25 42 14.25	0.251	0.254	2.384000	0.095	3.380000	0.091	15.068	14.900	7	0.598	0.591	13
RADJ001311+2556	00 13 11.4840	+25 56 41.98	0.121	0.124	4.782000	0.095	4.500000	0.076	14.915	14.203	150	0.295	0.281	16
RADJ001313+2545	00 13 13.0198	+25 45 15.15	1.579	1.757	0.358240	0.094	0.529620	0.155	17.375	11.916	36	4.588	3.147	28
RADJ001314+2541	00 13 14.6461	+25 41 14.85	0.745	0.804	0.723783	0.074	0.824690	0.121	14.606	13.296	162	1.909	1.738	16
RADJ001318+2604C1	00 13 18.8340	+26 04 38.76	1.284	1.093	0.578250	0.093	0.597710	0.156	22.405	9.339	128	3.666	1.528	7
RADJ001320+2604C2	00 13 20.1221	+26 04 11.43	0.052	0.051	12.512000	0.092	12.24000	0.081	17.148	14.930	130	0.129	0.113	2
RADJ001320+2556	00 13 20.5522	+25 56 55.59	0.588	0.715	0.911656	0.094	0.993930	0.154	17.319	11.884	151	1.797	1.233	11

TABLE 2—Continued

Name	RA(J2000) (h,m,s)	Dec(J2000) (° ′ ″)	$\sigma_{RA}$ (″)	$\sigma_{Dec}$ (″)	$S_P$ (mJy)	$\sigma_{S_P}$ (mJy)	$S_T$ (mJy)	$\sigma_{S_T}$ (mJy)	$\theta_M$ (″)	$\theta_m$ (″)	$PA$ (deg)	$\sigma_{\theta_M}$ (″)	$\sigma_{\theta_m}$ (″)	$\sigma_{PA}$ (deg)
RADJ001321+2543	00 13 21.4059	+25 43 49.37	0.693	0.709	0.800000	0.096	0.888660	0.148	14.764	13.115	140	1.745	1.551	10
RADJ001323+2600	00 13 23.5224	+26 00 29.25	0.038	0.038	15.877000	0.095	16.24000	0.097	15.258	15.080	130	0.091	0.090	21
RADJ001325+2553	00 13 25.9317	+25 53 37.18	0.564	0.700	1.170000	0.092	1.70000	0.210	22.747	14.340	30	1.791	1.129	7
RADJ001327+2543	00 13 27.2897	+25 43 35.07	1.293	1.224	0.424522	0.094	0.332500	0.119	13.870	12.706	64	3.091	2.832	13
RADJ001339+2543	00 13 39.8998	+25 43 54.55	0.187	0.189	3.140000	0.065	4.010000	0.161	14.983	14.384	141	0.451	0.433	30
RADJ001342+2546	00 13 42.2038	+25 46 18.76	2.952	1.554	0.361750	0.030	0.654340	0.237	27.823	14.628	92	6.953	3.656	15
RADJ001349+2539	00 13 49.1766	+25 39 20.08	0.424	0.355	1.519000	0.035	1.450000	0.162	16.018	13.413	88	0.998	0.835	14
RADJ001349+2609	00 13 49.9358	+26 09 25.19	0.104	0.103	6.301000	0.094	7.330000	0.088	17.944	14.591	46	0.268	0.218	3
RADJ001350+2608	00 13 50.7426	+26 08 06.93	1.314	1.047	0.460249	0.094	0.364860	0.110	15.341	11.627	107	3.153	2.390	30
RADJ001355+2540	00 13 55.6385	+25 40 48.82	1.129	1.151	0.538649	0.094	0.547750	0.165	16.771	13.643	138	2.945	2.396	34
RADJ001355+2553	00 13 55.8745	+25 53 27.52	0.738	0.727	0.760000	0.097	1.432330	0.135	15.362	12.182	133	1.912	1.516	22
RADJ001359+2601	00 13 59.7647	+26 01 23.68	0.414	0.394	1.413000	0.095	1.260000	0.035	15.092	13.286	124	1.011	0.890	21
RADJ001359+2605	00 13 59.9453	+26 05 17.72	0.498	0.632	1.080000	0.095	1.090000	0.087	17.033	13.351	175	1.492	1.169	14
RADJ001401+2559C1	00 14 01.5445	+25 59 59.45	0.066	0.071	9.410000	0.094	0.860000	0.082	17.264	15.048	150	0.173	0.151	3
RADJ001401+2610	00 14 01.8256	+26 10 59.96	1.142	1.042	0.465686	0.084	0.329440	0.120	13.499	11.792	114	2.742	2.395	31
RADJ001403+2559C2	00 14 03.1629	+25 59 37.11	0.080	0.081	8.005000	0.088	9.080000	0.028	16.501	15.463	140	0.195	0.182	7
RADJ001405+2551	00 14 05.6756	+25 51 29.74	0.373	0.305	1.884000	0.095	2.100000	0.081	17.524	14.319	90	0.879	0.719	10
RADJ001408+2550	00 14 08.0579	+25 50 37.67	0.504	0.471	1.172000	0.035	1.650000	0.072	14.896	13.522	113	1.202	1.091	24
RADJ001410+2610	00 14 10.9098	+26 10 35.97	0.325	0.308	1.828000	0.095	1.170000	0.085	15.161	13.586	60	0.785	0.703	19
RADJ001411+2546	00 14 11.0172	+25 46 03.46	0.230	0.203	2.919000	0.095	3.190000	0.110	16.703	14.714	93	0.541	0.477	10
RADJ001411+2541	00 14 11.8566	+25 41 24.11	1.191	1.401	0.417457	0.088	0.331760	0.140	14.811	12.073	19	3.356	2.736	45
RADJ001416+2610	00 14 16.8121	+26 10 51.50	0.862	0.944	0.681037	0.093	0.696850	0.126	16.754	13.742	149	2.327	1.909	28
RADJ001418+2540	00 14 18.7695	+25 40 08.27	0.499	0.540	1.107000	0.095	1.200000	0.110	15.381	13.182	150	1.314	1.126	12

TABLE 3  
OPTICAL-INFRARED DATA

Name	RA(J2000) <sup>a</sup> (h,m,s)	Dec(J2000) <sup>a</sup> (° / ' / '')	$\delta_{radio-opt}$ ( $''$ )	$\log(LR)$	$P_{rad}(\min, \max)^c$	$r$	$J(\sigma_J)^b$	$H(\sigma_H)$	$K(\sigma_K)$	$r - H$	$r - K$	morph <sup>c</sup>
RADJ001216+2601 <sup>d</sup>	00 12 16.530	+26 01 32.77	7.41	-4.163	$\ll 0.1$	24.083(?)	> 17.434	> 17.608	16.345(0.460)	< 6.475(?)	7.743(?)	?
RADJ001216+2543	00 12 16.783	+25 43 01.34	1.31	3.537	$\approx 1$	17.565	> 18.792	15.144(0.102)	> 17.029	2.421	< 0.536	E
RADJ001217+2602	00 12 17.280	+26 02 54.85	1.78	1.514	0.969	22.057	...	...	...	...	...	E
RADJ001218+2554	...	...	...	...	> 25	...	...	...	...	...	...	...
RADJ001227+2543	00 12 27.033	+25 43 41.19	3.09	0.685	0.793,0.828	22.971	...	...	...	...	...	Irr
RADJ001237+2607	00 12 37.248	+26 07 48.49	0.39	2.883	$\approx 1$	19.371	> 16.452	16.248(0.269)	> 15.242	3.123	< 4.129	S
RADJ001242+2600 <sup>d</sup>	00 12 42.347	+26 00 30.83	3.42	0.278	0.472,0.654	23.621(?)	...	...	...	...	...	?
RADJ001243+2558	...	...	...	...	> 25	> 18.628	> 17.557	17.096(1.098)	?	> 7.904	?	...
RADJ001246+2543	00 12 45.777	+25 43 50.59	3.83	1.293	0.949,0.951	21.169	...	...	...	...	...	E
RADJ001247+2602 <sup>d</sup>	00 12 47.889	+26 02 35.96	4.03	0.302	0.501,0.670	22.768(?)	...	...	...	...	...	E
RADJ001250+2550	00 12 50.137	+25 50 10.86	1.52	1.225	0.940,0.943	23.128	...	...	...	...	...	E
RADJ001252+2549	00 12 51.969	+25 49 38.81	0.65	2.919	$\approx 1$	18.984	17.416(0.285)	16.057(0.204)	> 16.321	2.927	< 2.663	E
RADJ001254+2600 <sup>d</sup>	00 12 54.855	+26 00 44.70	3.83	0.246	0.432,0.640	23.004(?)	...	...	...	...	...	?
RADJ001255+2541 <sup>d</sup>	00 12 55.064	+25 41 54.13	4.56	-0.689	$\ll 0.1$	23.559(?)	...	...	...	...	...	?
RADJ001257+2559	00 12 57.287	+25 59 43.60	0.03	2.248	0.994	20.384	17.066(0.210)	16.131(0.225)	> 15.178	4.253	< 5.206	S
RADJ001259+2607	00 12 59.187	+26 07 19.09	1.21	2.706	0.998	19.010	> 15.303	15.541(0.144)	> 13.985	3.469	< 5.025	S
RADJ001300+2556	00 13 01.007	+25 56 57.08	0.35	1.505	0.969	22.974	...	...	...	...	...	Irr
RADJ001303+2602	00 13 03.204	+26 02 07.27	0.31	1.681	0.979	22.492	...	...	...	...	...	E
RADJ001304+2544	...	...	...	...	> 25	...	...	...	...	...	...	?
RADJ001305+2607	00 13 05.293	+26 07 53.81	1.60	1.675	0.979	21.835	> 16.403	16.118(0.207)	> 14.996	5.717	< 6.839	E
RADJ001307+2542	...	...	...	...	> 25	...	...	...	...	...	...	...
RADJ001311+2556	00 13 11.603	+25 56 41.19	1.95	1.515	0.969	21.950	...	...	...	...	...	Irr
RADJ001313+2545	00 13 13.049	+25 45 17.44	2.33	0.778	0.833,0.857	23.464	...	...	...	...	...	?
RADJ001314+2541	00 13 14.595	+25 41 14.73	0.78	1.118	0.924,0.930	23.698	...	...	...	...	...	?
RADJ001318+2604	00 13 18.794	+26 04 37.24	1.64	1.189	0.935,0.940	22.847	...	...	...	...	...	Irr
RADJ001320+2604	00 13 20.199	+26 04 10.69	1.37	1.706	0.980	21.938	...	...	...	...	...	E
RADJ001320+2556	00 13 20.705	+25 56 53.85	2.88	1.647	0.977	20.481	> 18.633	16.550(0.348)	> 15.359	3.931	< 5.122	E
RADJ001321+2543	00 13 21.339	+25 43 48.81	1.15	0.996	0.899,0.908	23.929	17.526(0.323)	> 17.663	> 17.017	< 6.266	< 6.912	?
RADJ001323+2600 <sup>d</sup>	00 13 23.256	+26 00 27.73	4.28	0.247	0.433,0.638	24.040(?)	...	...	...	...	...	?
RADJ001325+2553	00 13 25.803	+25 53 39.14	2.75	0.695	0.798,0.832	23.650	...	...	...	...	...	?
RADJ001327+2543	00 13 27.260	+25 43 33.55	1.58	1.265	0.946,0.950	22.639	...	...	...	...	...	E
RADJ001339+2543	...	...	...	...	> 25	...	...	...	...	...	...	...
RADJ001342+2546 <sup>d</sup>	00 13 41.666	+25 46 16.96	8.27	0.238	0.421,0.633	21.194(?)	...	...	...	...	...	Irr
RADJ001350+2608	00 13 50.572	+26 08 12.05	4.73	0.617	0.758,0.805	22.178	...	...	...	...	...	E
RADJ001353+2553	00 13 55.857	+25 53 28.22	0.75	3.729	$\approx 1$	17.286	15.642(0.071)	14.756(0.082)	14.419(0.098)	2.53	2.867	E
RADJ001359+2601	...	...	...	...	> 25	...	...	...	...	...	...	...
RADJ001359+2605 <sup>d</sup>	00 13 59.795	+26 05 22.01	4.84	-0.760	$\ll 0.1$	23.763(?)	...	...	...	...	...	?
RADJ001401+2559	00 14 01.559	+25 59 57.15	2.31	0.861	0.862,0.878	23.390	...	...	...	...	...	?
RADJ001403+2559 <sup>d</sup>	00 14 03.088	+25 59 33.06	4.20	-0.790	$\ll 0.1$	24.707(?)	...	...	...	...	...	?
RADJ001405+2551	00 14 05.728	+25 51 28.88	1.16	1.893	0.987	21.508	...	...	...	...	...	E
RADJ001408+2550	...	...	...	...	> 25	...	...	...	...	...	...	...
RADJ001411+2546	...	...	...	...	> 25	...	...	...	...	...	...	...
RADJ001411+2541	00 14 11.805	+25 41 22.34	1.93	1.016	0.904,0.912	23.164	...	...	...	...	...	?

<sup>a</sup>Refers to optical position.

<sup>b</sup>Values with ">" are 2 $\sigma$  upper limits on measured fluxes, otherwise, errors are quoted in parenthesis.

<sup>c</sup>Optical morphology: E—Elliptical, Irr—Irregular or Disturbed, S—Spiral, ?—Unknown.

<sup>d</sup>Optical identification uncertain due to either extended radio emission and large offset from radio centroid position, or low  $P_{rad}$ .

<sup>e</sup>Limits on the probability that the optical candidate is the "true" identification. Cases with very low or very large  $\log(LR)$  are listed with  $P_{rad}(\max) \ll 0.1$  or only  $P_{rad}(\min)$  respectively (see eq.[4]).

Table 4. Population synthesis models

Type	SFR( $t$ )	IMF	Age (Gyr) <sup>a</sup>
E/SO	$\tau_1^{-1} \exp(-t/\tau_1)$	Scalo	12.7
Sab/Sbc	$\tau_8^{-1} \exp(-t/\tau_8)$	Scalo	12.7
Scd/Sdm	constant	Salpeter	12.7
SB	constant	Salpeter	0.1

<sup>a</sup>For the SB-type, an age of 0.1 Gyr is assumed to apply at all redshifts. For other types, this refers to the present day age.

## REFERENCES

Benn, C. R., Rowan-Robinson, M., McMahon, R. G., Broadhurst, T. J., & Lawrence, A., 1993, MNRAS, 263, 98

Blain, A. W., Smail, I., Ivison, R. J., & Kneib, I. -P., 1999, MNRAS, 302, 632

Bruzual, A. G., & Charlot, S., 1993, ApJ, 405, 538

Calzetti, D. Kinney, A. L., & Storchi-Bergmann, T., 1996, ApJ, 458, 132

Ciliegi, P., McMahon, R. G., Miley, G., Gruppioni, C., Rowan-Robinson, M. et al., 1999, MNRAS, 302, 222

Condon, J. J., 1989, ApJ, 338, 13

Condon, J. J., & Yin, Q. F., 1990, ApJ, 357, 97

Condon, J. J., 1992, A&A Rev., 30, 575

Condon, J. J., 1997, PASP, 109, 166

Condon, J. J., Cotton, W. D., Greison, E. W., Yin, Q. F., Perley, R. A., Taylor, G. B., & Broderick, J. J., 1998, AJ, 115, 1693

Cram, L. E., 1998, ApJ, 506, L85

Cram, L. E., Hopkins, A. M., Mobasher, B., & Rowan-Robinson, M., 1998, ApJ, 507, 155

Danese, L., De Zotti, G., Franceschini, A., & Toffolatti, L., 1987, ApJ, 318, L15

de Ruiter, H. R., Willis, A. G., & Arp, H. C., 1977, A&AS, 28, 211

Devriendt, J. E., Guiderdoni, B., & Sadat, R., 1999, A&A, 350, 381

Djorgovski, S., Soifer, B. T., Pahre, M. A., Larkin, J. E., Smith, J. D. et al., 1995, *ApJ*, 438, L13

Downes, A. J. B., Peacock, J. A., Savage, A., & Carrie, D. R., 1986, *MNRAS*, 218, 31

Dunlop, J., Peacock, J., Spinrad, H., Dey, A., Jimenez, R., Stern, D., & Windhorst, R., 1996, *Nature*, 381, 581

Fanaroff, B. L., & Riley, J. M., 1974, *MNRAS*, 167, 31

Georgakakis, A., Mobasher, B., Cram, L., Hopkins, A., & Lidman, C., 1999, *MNRAS*, 306, 708

Genzel, R., Lutz, D., Sturm, E., Egami, E., Kunze, D., Moorwood, A. F. M., Rigopoulou, D., Spoon, H. W. W., Sternberg, A., Tacconi-Garman, L. E., Tacconi, L., and Thatte, N., 1998, *ApJ*, 498, 579

Goudfrooij, P., & de Jong, T., 1995, *A&A*, 298, 784

Gruppioni, C., Mignoli, M., & Zamorani, G., 1998, *MNRAS*, 304, 199

Haarsma, D. B., & Partridge, R. B., 1998, *ApJ*, 503, L5

Haarsma, D. B., Partridge, R. B., Waddington, I., & Windhorst, R. A., 1999, 19th Texas Symposium on Relativistic Astrophysics and Cosmology, Paris 1998, ed. J. Paul, T. Montmerle, & E. Aubourg (CEA Sarclay), 600

Hammer, F., Crampton, D., Lilly, S. J., Le Fèvre, O., & Kenet, T., 1995, *MNRAS*, 276, 1085

Helou, G., Soifer, B. T., & Rowan-Robinson, M., 1985, *ApJ*, 298, L7

Hopkins, A. M., Mobasher, B., Cram, L., & Rowan-Robinson, M., 1998, *MNRAS*, 296, 839

Kells, W., Dressler, A., Sivaramakrishnan, A., Carr, D., Koch, E., Epps, H., Hilyard, D., & Pardeilhan, G., 1998, PASP, 110, 1487

Kron, R. G., Koo, D. C., & Windhorst, R. A., 1985, A&A, 146, 38

Lilly, S. J., 1989, ApJ, 340, 77

Lonsdale, C. J., Conrow, T., Evans, T., Fullmer, L., Moshir, M., Chester, T., Yentis, D., Wolstencroft, R., MacGillivray, H., & Egret, D., 1998, New Horizons From Multi-Wavelength Sky Surveys, Proc. IAU Colloquium 179, Johns Hopkins University, ed. B. McLean, D. Golombek, J. Hayes, & H. Payne, Kluwer Academic Publishers, p. 450

Lutz, D., Spoon, H. W. W., Rigopoulou, D., Moorwood, A. F. M., Genzel, R., 1998, ApJ, 505, L103

Madau, P., Ferguson, H. C., Dickinson, M. E., Giavalisco, M., Steidel, C. C., & Fruchter A., 1996, MNRAS, 283, 1388

Madau, P., Pozzetti, L., Dickinson, M., 1998, ApJ, 498, 106

McCarthy, P. J., Persson, S. E., & West, S. C., 1992, ApJ, 386, 52

Meurer, G., Heckman, T. M., Lehnert, M. D., Leitherer, C., & Lowenthal, J., 1997, AJ, 114, 54

Mobasher, B., Cram, L., Georgakakis, A., & Hopkins, A., 1999, MNRAS, 308, 45

Nakata, F., Shimasaku, K., Doi, M., Kashikawa, N., Kawasaki, W. et al., 1999, MNRAS, 309, L25

Norris, R. P., Allen, D. A., & Roche, P. F., 1988, MNRAS, 234, 773

Oort, M. J. A., 1987, A&AS, 71, 221

Peacock, J. A., 1993, Extragalactic Background Radiation: A Meeting in Honour of Riccardo Giacconi, Proc. Space Telescope Science Institute, ed. D. Calzetti, M. Livio & P. Madau, Cambridge University Press, p. 237

Pei, Y. C., 1992, ApJ, 395, 130

Prestage, R. M., & Peacock, J. A., 1983, MNRAS, 204, 355

Richards, E. A., Fomalont, E. B., Kellermann, K. I., Windhorst, R. A., Partridge, R. B., Cowie, L. L., Barger, A. J., 1999, ApJ, 526, L73

Richards, E. A., 2000, astro-ph/9908313, To appear in ApJ

Rowan-Robinson, M., Benn, C. R., Lawrence, A., McMahon, R. G., & Broadhurst, T. J., MNRAS, 263, 123

Sanders, D. B., & Mirabel, I. F., 1996, ARA&A, 34, 749

Schaerer, D., 1999, astro-ph/9906014, To appear in Building the Galaxies: from the Primordial Universe to the Present, XIXth Moriond astrophysics meeting, F. Hammer et al. (eds.), Editions Frontieres (Gif-sur-Yvette)

Scoville, N. Z., Sargent, A. I., Sanders, D. B., & Soifer, B. T., 1991, ApJ, 366, L5

Serjeant, S., Gruppioni, C., & Oliver, S., 1999, preprint astro-ph/9808259

Smith, H. E., Lonsdale, C. J., Lonsdale, C. J., & Diamond, P. J., 1998a, ApJ, 493, 17

Smith, H. E., Lonsdale, C. J., Lonsdale, C. J., & Diamond, P. J., 1998b, BAAS, 192, 1110

Stetson, P. B., 1987, PASP, 99, 191

Sutherland, W., & Saunders, W., 1992, MNRAS, 259, 413

Thompson, D., Beckwith, S. V. W., Fockenbrock, R., Fried, J., Hippelein, H. et al., 1999,  
ApJ, 523, 100

Thuan, X. T., & Gunn, J. E., 1976, PASP, 88, 543

Thuan, X. T., & Condon, J. J., 1987, ApJ, 322, L9.

Thuan, X. T., Windhorst, R. A., Puschell, J. J., Isaacman, B. R., & Owen, F. N., 1984,  
ApJ, 285, 515

Windhorst, R. A., Miley, K. G., Owen, F. N., Kron, R. G., & David, C. K., 1985, ApJ, 289,  
494

Windhorst, R. A., Fomalont, E. B., Partridge, R. B., Lowenthal, J. D., 1993, ApJ, 405, 498

This figure "fig2.png" is available in "png" format from:

<http://arxiv.org/ps/astro-ph/0002490v1>

This figure "fig81.png" is available in "png" format from:

<http://arxiv.org/ps/astro-ph/0002490v1>

This figure "fig82.png" is available in "png" format from:

<http://arxiv.org/ps/astro-ph/0002490v1>

This figure "fig83.png" is available in "png" format from:

<http://arxiv.org/ps/astro-ph/0002490v1>